University of Dundee

MASTER OF SCIENCE

Mechanical characterisation of soft biological tissue by using surface acoustic waves

Li, Sinan

Award date:
2011

MASTER OF SCIENCE

Mechanical characterisation of soft biological tissue by using surface acoustic waves

Sinan Li

2011

University of Dundee

Mechanical Characterisation of Soft Biological Tissue by Using Surface Acoustic Waves

Mr Sinan Li

BEng

Submitted for the Degree of Master of Science in Biomedical Engineering

School of Engineering, Physics and Mathematics
College of Art, Science and Engineering
University of Dundee,

Dec 2011

Dedication

This work is dedicated to my admired and beloved parents.

Thank you for your love, understanding, and support throughout my life and study.

Acknowledgement

I would like to take this opportunity to express my deepest gratitude to my research supervisor Dr. Zhihong Huang, who has really helped me a lot all though the whole program of '3+1+1', both in research and offering me the best resource and opportunity to present myself in the best possible light. I also thank Dr. Huang for her great efforts to provide me financial supports for the MSc study and the attendance in international academic conferences. It is she who leads me into the academic and cultivated me to allow for a progressive PhD study.

I would also like to thank Ms. Chunhui li, the research partner who helped me the most in the research project. Even though she is visiting United States during the past years, whenever I got problems and difficulties she always listened to me and helped me with her great patience. She would also like to share me the new ideas and findings in the research and guide me to the right path with her best known knowledge.

I would like to acknowledge my girlfriend Miss Yi Cheng for supporting and encouraging me and putting up with the neglect along with the highs and lows for my whole MSc study. I also appreciate for your discuss and help in the whole research progress and in life. I love you more than I can say.

Thanks also go to Mr. Cheng Wei, Mr. Xu Xiao, Mr. Yongqiang Qiu, Mr. Yang Kuang, Mr. Qiang Wen, Mr. Jiang You, Mr. Han Wang, Mr. Rui Cao, Mr. Yuwei Jin, Miss Jing Gao and Miss Zhen Qiu for your every little helps in research and bringing joy and happiness to my life in Dundee. Wish you all going well in your current study and future career life!

Thanks also go to Prof. Sandy Cochran for his advices to this project in the routine weekly group meeting.

Finally I would like to thank my mum and dad for your meticulous supports and cares all through the way. Your son will go ahead as always and pay back to your deepest love to me.

Declaration

I declare that I am the author of this dissertation. All the references cited in this thesis have been consulted by me except those in table 2-1 are consulted from ref [17]. This dissertation is a record of the works I have been done during the MSc study at University of Dundee. The content has not been previously accepted for a higher degree.

Table of Contents

Dedication I

Acknowledgement II

Declaration III

List of Figure VII

List of Tables IX

Abstract X

Chapter 1 Introduction 1

Background 1

Dissertation structure 3

Chapter 2 Literature Review 4

2.1 Elasticity in soft tissue 4

2.1.1 Overview 4

2.1.2 Elasticity modulus and measurement 4

2.2 Elasticity measurement 7

2.2.1 Static and dynamic excitation methods 8

2.2.2 External excitation methods 8

2.2.3 Internal excitation methods 9

2.2.4 Detection methods for elastography 10

2.2.5 Limitation in skin characterisation 10

2.3 Surface acoustic wave generation and detection 11

2.3.1 Surface acoustic waves 11

2.3.2 Surface acoustic wave generation 12

2.3.3 Surface acoustic wave detection 17

Chapter 3 FE simulation of tissue characterisation by SAWs 23

Introduction 23

3.1 Finite element method 23

3.1.1 Finite element method 23
3.1.2 Introduction of ANSYS 24
3.2 Simulation of laser generation of SAWs 24
3.2.1 Model creation 24
3.2.2 Model mesh 26
3.2.3 Governing equation 28
3.3 Boundary conditions 29
3.3.1 Thermal boundary conditions 29
3.3.2 Mechanical boundary conditions 31
3.3.3 Solution control 32
3.4 Result and discussion 33
3.4.1 Sensing lateral elasticity change by SAWs 36
3.4.2 Calculation of phase velocity 41
3.4.3 Sensing vertical elasticity change by SAWs 42
3.5 Conclusion 43
Chapter 4 Experimental study of using SAWs to characterise tissue 44
Introduction 44
4.1 Experiment platform 44
4.1.1 Tissue mimicking phantom fabrication 45
4.1.2 SAWs generation 46
4.1.3 SAWs detection 47
4.1.4 Scanning scheme 48
4.2 Results in Homogeneous TMM phantoms 49
4.2.1 SAWs signal in time and spectrum 49
4.2.2 Phase velocity of SAWs on soft TMM phantoms 51
4.2.3 Simplified relationship between SAWs velocity and elasticity 51
4.2.4 Verification of elasticity measurement 52
4.2.5 Measurement bias in soft and hard TMM phantom 55

4.3 Results on two-layer heterogeneous TMM phantom 56
4.3.1 Temporal and spectrum of SAWs in two-layer TMM phantom 56
4.3.2 Phase velocity of SAWs in two-layer TMM phantom. 57
4.4 Results in ex-vivo biological tissue 59
4.5 Conclusion 60
Chapter 5 Conclusion and future work 62
5.1 Conclusion 62
5.2 Future work 63
References 65
Appendix A 70
Appendix B 78
Appendix C 89

List of Figure

Figure 2- 1 Typical stress-strain relation in soft biological tissues [15] 5

Figure 2- 2 Schematic view of surface acoustic wave and the orbit of particle movement. 11

Figure 2-3 Refraction of acoustic waves cause the acoustic mode conversion [71] 14

Figure 2-4 Typical structure of an edge ultrasonic transducer [71] 15

Figure 2-5 Working principle of EMAT for the generation of SAWs [72].. 15

Figure 2-6 Laser generation of acoustic waves in thermo-elastic regime (a) ablative regime (b) [76] 16

Figure 2-7 Basic structures of piezo-electric transducer 18

Figure 2- 8 Piezoelectric effect and Electrostriction effect. 19

Figure 2-9 Working principle of Fibre Bragg grating. [77] 20

Figure 2-10 Interferometric system as optical detection of ultrasound: wavefront integration technique interferometer (A), Michelson surface displacement interferometer (B) [77]. 21

Figure 2- 11 Basic structure of laser vibrometer system 22

Figure 3- 1 Schematic of model in Ansys ……....26

Figure 3- 2 Model was divided into 16 sections to refine the grids size 28

Figure 3- 3 Schematic of the electro-magnetic fields of a laser beam in a Gauss spatial mode 30

Figure 3- 4 Schematic of signal detection and location. 34

Figure 3- 5 Typical waveform of laser generated SAWs. 34

Figure 3- 6 SAWs signals and the echoes reflected from elastic boundary 35

Figure 3- 7 Typical spectrum of simulated SAWs. 36

Figure 3- 8 SAWs (out of plane displacement) detected in sequence on model 37

Figure 3- 9 Peak to peak amplitude of SAWs 38

Figure 3- 10 SAWs signals plotted at different scales. 39

Figure 3- 11 SAWs group velocity trend 40

Figure 3- 12 SAWs phase velocity on soft tissue and hard tissue 42

Figure 4- 1 Schematic of experiment platform……..... 46

Figure 4- 2 Fabricated TMM agar phantoms made with 1% (1), 2% (2), 3% (3) agar concentration in weight 46

Figure 4- 3 Line-source design: a bar attached to shaker head to enhance the SAWs signal strength to get good SNR 47
Figure 4- 4 Laser vibrometer head (Polytec, OFV-534) 47
Figure 4- 5 Schematic of shaker alignment with detection points. 48
Figure 4- 6 Scanning system 49
Figure 4- 7 Typical SAWs waveforms that were detected on 1% agar TMM phantom 50
Figure 4- 8 Typical spectrum of SAWs on 1% agar phantom and their cross-correlation spectrum. 50
Figure 4- 9 SAWs phase velocity on homogeneous agar phantoms 51
Figure 4- 10 Compression test platform (Tinius Olsen H5KS) 53
Figure 4- 11 Stress-strain plot from the compression test to measure the phantoms elasticity 53
Figure 4- 12 Comparison of Young's modulus measured from SAWs phase velocity and independent compression test 54
Figure 4- 13 Relation between phase velocity and the concentration and stiffness of phantom. 54
Figure 4- 14 SAWs phase velocity on 1%, 2% and 3% agar phantoms 56
Figure 4- 15 SAWs waveform in heterogeneous agar phantom. 57
Figure 4- 16 Frequency responses of SAWs in heterogeneous agar phantom 57
Figure 4- 17 SAWs phase velocity in two-layer heterogeneous agar phantom. 59
Figure 4- 18 Phase velocity of SAWs in an ex-vivo pig liver. 60
Figure 4- 19 High frequency ultrasound B-scan image showing the longitudinal-section of pig liver. 60

List of Tables

Table 2- 1 Young's modulus of various types of human tissue from the published data [16]..... 7
Table 3- 1 Thermal and elastic properties of finite element model…… ...26
Table 3- 2 Optical parameters of different lasers in tissue..... 32
Table 3- 3 Summary of the parameters for the definition of boundary conditions..... 33
Table 3-4 Comparison between Young's modulus measured from SAWs group velocity and the values originally specified in model 40
Table 4-1 Young's modulus (E) measured from SAWs phase velocity and the independent compression test……. …….……..53
Table 4-2 Mechanical properties of pig liver measured by SAWs phase velocity. 60

Abstract

Mechanical properties are important parameters in assessing physiologic conditions of biologic tissue for medical diagnosis or disease progression tracking. Surface acoustic waves (SAWs) have been preliminarily used for the characterisation of tissue mechanical properties and it is increasingly becoming a topic of research interest as SAWs can provide more localised information in the tissue near-surface region which is particular advantaged for the clinical diagnosis of skin malignant diseases, such as carcinoma cutaneum and scleroderma. This dissertation further exploited the use of surface acoustic waves in the tissue mechanical characterisation, it takes a novelty approach in applying SAW for a precise mechanical characterisation of layered soft tissue, in terms of both stiffness characterisation and thickness evaluation. There are the two main contributions reported and discussed in this dissertation:

Firstly, from a validated numeric analysis of acoustic wave propagation, SAWs have been found to be highly sensitive to the elasticity variation distributed along the surface of tissue sample; an immediate, dramatic change of both attenuation and velocity of surface acoustic waves were observed at the tissue elasticity boundaries. These results can be used to get a rapid locating and quantification of the abnormalities along the tissue superficial layer. Secondly, investigation of using SAWs was also reported for evaluation of vertical elasticity variations at depth of tissue by analysing the phase velocity and taking consideration of the surface wave penetration attributes. Using an advanced method for generating a robust surface wave signal with eliminated perturbations, SAWs found to be not only capable to do an accurate quantification of the stiffness in a layered structure, but also can provide reliable characterisation of the thickness of the superficial layer. Results were obtained and calibrated on tissue mimicking phantoms and further validated on *ex-vivo* biologic tissues.

Chapter 1 Introduction

Background

Tissue mechanical properties are important parameters for understanding patho-physiology, and in many cases to improve medical diagnosis, physicians rely greatly on quantitative measures and comprehensive analysis of soft tissues. A typical example is the diagnosis of scleroderma, a multisystem disease featured by thickening and hardening human skin and even the internal organ. At present, manual palpation is one of the primary means for diagnosis and examination of scleroderma. Practitioners sense the stiffness and thickness of target by simply pressing or knocking patient skin. Even though it is indispensable in medical diagnosis, palpation does have its limitations mainly because the evaluation is not quantitative and the interpretation is totally subjective. Therefore, more reliable diagnosis and examination always goes to biopsy, which is invasive and can lead soreness and discomfort to patients. For above reasons, this dissertation aims to develop a novel method that can non-invasively characterise the mechanical properties of human skin to aid the diagnosis and examination of scleroderma by quantitative stiffness and thickness measurements.

A few modalities have been developed for non-invasive characterisation of tissue, such as ultrasound elastography [1-3], acoustic radiation force impulse elastography (ARFIE) [4, 5] and magnetic resonance elastography (MRE) [6, 7], etc. Quantitative stiffness measurement or imaging by above methods normally relies on tracking shear wave speeds. However, shear waves may have limitations for characterising skin since shear waves spread in the bulk of tissue and can only provide reliable stiffness evaluations for the bulk tissues. Compared with this, surface acoustic waves (SAWs) have superiority in skin characterisation since SAWs spread on surface and most of the wave energy localised in skin. In addition, SAWs penetration is comparable to the wavelength: for broadband SAWs, the low frequency contents penetrate deeper and the speed is determined by the subtractive structure, while high frequency contents penetrate superficially and the speed is determined by the surface structure. Therefore by looking at SAWs speed at different frequencies (SAWs phase velocity dispersion), different structures within or underneath skin can be characterised. This is the principle idea all through this dissertation.

There are two mechanisms usually used to generate surface acoustic waves in biological tissues, either by delivering direct mechanical impulses on surface or by thermal-elastic excitation using a laser pulse. Both of these two methods have attracted research interests for

tissue characterisation in recent years. Zhang etc [8, 9] used an electro-magnetic shaker to generate SAWs on human skin. In their works, narrow band SAWs from 100 *Hz* to 400 *Hz* were detected, and SAWs phase velocity at these relatively low frequencies were fitted within the Voigt's model [10, 11] which links elasticity and viscosity parameters of a medium to acoustic wave velocity dispersions [12] . On the other hand, Li etc. [13, 14] generated SAWs in tissue mimicking phantoms by photo-acoustic techniques where SAWs were generated through thermal-elastic regime as a result of the localised heating induced from tissue absorption of laser energy. Phantoms in the study were made as two layers with varied stiffness. By analysing phase velocity of SAWs in a relatively broad spectrum (up to several kHz), phantom elasticity in both surface layer and subtractive layer were inversed out.

However, improvements and further studies need to be carried on for both research streams. In fact, at such low frequencies (100-400 *Hz*) in Zhang's work, SAWs penetrated at least a few millimetres underneath tissue surface, far away beyond the epidermis and dermis layers (typically 0.08 mm and 1.0 mm in thickness respectively) in skin and reached the subcutaneous fat. As a result, fitting SAWs speeds with Voigt's model at low frequencies can hardly provide localised skin characterisation since SAWs penetrated too deep and thus cannot provide any unique information of superficial structures such as epidermis and dermis layer in human skin. Compared with Zhang's work, Li etc. extended the use of SAWs to characterise layer-featured samples by broadening SAWs frequency to kHz range. However the results were based on tissue mimicking (TMM) phantoms, and no data from real biological tissues were presented whose superficial structures are much thinner than the TMM ones. Moreover, neither of them investigated the presence of lateral stiffness change in their samples (skin was treated as homogenous in Zhang's work and phantoms were heterogeneous at depth but homogeneous in lateral in Li's work) nor using SAWs to make a thickness measurement of superficial layers. This dissertation may contribute to fill in this gap.

Therefore the aim of this project is first to explore using SAWs to characterise a tissue model with both lateral and vertical elasticity change, and then validate the elasticity and superficial layer thickness measurement by experiments in realistic biological samples.

Dissertation structure

Chapter 1 gives an introduction of the project, including background of current research, aim and objective of this project and brief structure of the dissertation.

Chapter 2 is a literature review of the background and theories used in this work. Contents include biological tissue elasticity, methods for elasticity measurement, introduction of SAWs, and SAWs generation and detection methods.

Following Li's work, simulation of tissue characterisation by laser generated SAWs is studied in chapter 3 with finite element method (FEM). Results from FE simulation were analysed and discussed, finished with a summary of the chapter.

In chapter 4, results and supposes from simulation were validated and strengthened by experiments. Experimental setups were introduced first in this chapter. Results on homogenous TMM phantoms, two-layer heterogeneous TMM phantom and ex-vivo biological tissues were presented and analysed in sequence to validate the conclusions drew from the simulation. Also, an independent mechanical test and thickness measurement were conducted to compare with the results evaluated from SAWs phase velocity. At last a summary of this chapter was given.

The results was summarised in the chapter 5, together with an outlook of the future works. At the end of dissertation, references and appendix were attached for the information that was not described in the text, such as simulation codes, signal acquisition platform, and also signal processing codes.

Chapter 2 Literature Review

In this chapter, elasticity of soft tissue and current modalities of elasticity measurement will be reviewed firstly, and then SAWs, together with its generation and detection methods are reviewed later from both experiment and theory aspects.

2.1 Elasticity in soft tissue

2.1.1 Overview

There are five primary types of soft tissue: the epithelial tissue, which consists of cells that are collocated closely to form continuous sheets to serve as the linings of structures; the connective tissue, full of strands of collagen to sustain and support structures to the body; the parenchymal tissue, which is the functional tissues of organs; the muscle tissue, movement of which acts as a response to biological electrical signals; and finally the verve tissue, in which the biological electrical signals are generated and conducted.

Organs are biological structures containing at least two types of tissues functioning for a common purpose, which are of the greatest interest in the medical physiology research. Typical examples of organs are inclusive of brain, heart, breast, kidney, liver, and the skin which is considered as the largest organ spreading over the entire human physiological systems. The mechanical properties of organs cannot be realistically described in terms of simple agglomerations of homogeneous cells [15]. For example, the mechanical characterisation of skin does need to be considered in the context of multiple scales, as it contains three primary structures: epidermis layer, dermis layer and the subcutaneous fats. In addition, the biological tissue may also present an attribute of viscoelasticity, manifesting oneself as hysteresis on relaxation of stress. Other factors relevant to the mechanical properties of organ could be the ambient temperature, living environment (*in-vivo or ex-vivo*), and the age of organ tissues. Therefore, medical diagnosis from the view of mechanical characterisation needs to account for quite a few variables, and it could be much complicated. In this pilot study, we only concern the elasticity of tissue in this dissertation, and eliminate the influence of other factors.

2.1.2 *Elasticity modulus and measurement*

Elasticity describes the tendency to resume original condition when an object suffers deformation induced by forces. Figure 2- 1 shows the typical stress-strain tendency in soft

biological tissues where stress describes the force acting on unit area and strain describes the stress-induced deformation by using change in length per unit length. At first, strain increases rapidly against stress because free fluid infiltrated in tissue is being eliminated out. With continuous force application, stress-strain curve presents a relatively linear part over a small increase of stress. However, with further increase of stress, increase in strain gradually slows down since it approaches the limit of elasticity. Therefore, stress-strain relation can vary largely with different conditions, and generally, the linear part is usually used for an accurate estimation of the tissue elasticity.

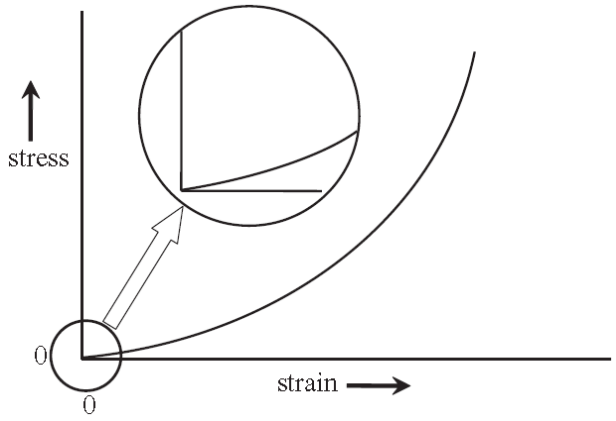

Figure 2- 1 Typical stress-strain relation in soft biological tissues [15]

The ratio of stress, σ, and strain, ε, is defined as elasticity. Direct product of stress/strain is known as Young's modulus, E, describing the longitudinal elasticity of a solid [15] .

$$\boldsymbol{\sigma = E \cdot \varepsilon} \tag{2- 1}$$

Besides this, Shear modulus and Bulk modulus are the other two terms frequently used to describe elasticity. Shear modulus describes the rigidity or torsion ability and the bulk modulus describes the volume elasticity. The relation between three elasticity modulus can be given by the following linear elastic constitutive equations [15]:

$$\boldsymbol{G = \frac{E}{(2+(1+\nu))}}, \tag{2- 2}$$

$$\boldsymbol{K = \frac{E}{(3(1-2\nu))}}, \tag{2- 3}$$

Note that E is the Young's modulus, G is the shear modulus, K is the bulk modulus, and ν is the Poisson's ratio.

Apart from stress-strain curve, tissue elasticity can be also estimated from measurement of acoustic wave speed by using equation (2-4) and equation (2-5) [15].

$$\boldsymbol{C_l = \sqrt{(\frac{K}{\rho})}}\,, \tag{2-4}$$

$$\boldsymbol{C_s = \sqrt{(\frac{G}{\rho})}}\,, \tag{2-5}$$

where C_l and C_s denote for the speed of longitudinal and shear wave that propagate in a material with density of ρ. There is no direct relationship between surface wave speed and solid elasticity modulus, however it can be derived from the solution of Rayleigh equation which gives a relationship between surface wave speed and shear wave speed. The derivation will be discussed in chapter 4.

Then elasticity modulus can be calculated from acoustic wave speed if density of material is known. Book [16] provides references of biological tissue parameters. In his review, longitudinal wave speed in soft tissue ranges from 1412 *m/s* to 1629 *m/s*, thought through both different sites of soft tissue such as the skin, tendon, cartilage, and the different conditions of soft tissue like normal and the diseased tissue. The corresponding values of density varied from 920 to 1060 kg/m^3. Therefore the bulk modulus of soft tissue can be estimated by substituting these values into equation (2-3). As a result, the bulk modulus ranges from ~1800 *MPa* to ~2800*MPa* in the soft biological tissues.

As stated above, three elasticity modulus can be transferable to each other by Poisson's ratio (equation 2-2 and 2-3). In soft tissues, Possion's ratio is usually in the range of 0.490 to 0.499 as biological tissues are hardly compressible. Substituting this to equation (2-2), relation between Young's modulus and shear modulus can come down to an easier form [15]:

$$\boldsymbol{E \approx 3G,} \tag{2-6}$$

indicating that shear modulus approximately equals one third of the Young's modulus. This approximation can be used for a convenient transfer of Young's modulus to shear modulus, and also the vice versa.

It has been reported in [17] that, shear and Young's modulus of different soft tissues varied over a few orders of magnitude, however, the change in the bulk modulus is no more than one order of magnitude. This makes it difficult to characterise tissue mechanical properties by using traditional ultrasound imaging with longitudinal waves. As Young's modulus is frequently used in literatures it is chosen to evaluate the mechanical properties of tissue in

this dissertation. The Table 2- 1 listed Young's modulus of various types of tissues, offering a basic perception of the Young's modulus values in biological soft tissues.

Table 2- 1 Young's modulus of various types of human tissue from the published data [15]

Tissue	Type	E (kPa)	Tissue	Type	E (kPa)
breast	unspecified	29 [18] 21 – 23 [20]	**Kidney**	unspecified	10 [19] 6 [20]
	adipose	19 [21]			13 [22]
	glandular	33 [21]			10 – 17 [23]
	fibrous	110 [21] 1.8 [24] 14 – 16 [20]		unspecified	7 – 10 [20] 1 – 3 [25] 0.4 - 1.7 [26]
	unspecified	10 – 40 [25] 7 – 57 [28]		normal	10 [27] 0.6 - 1.1 [29]
muscle	intercostal	1.2 – 1.8 [26] 100 [27]	**Liver**	focal nodular hyperplasia	1.2 - 2.5 [29]
	cardiac (systole)	100 [30]		chronic hepatitis	35 [22]
	intercostal	100 [27]		cirrhosis	52 [22] 1.2 - 4.9 [29]
	cardiac (diastole)	10 [30]		Cholangio-carcinoma	3 – 12 [29]
thrombus	unspecified	8 – 38 [31]		VX2 Ca	0.3 – 0.9 [25]

2.2 Elasticity measurement

Elastography is the technique that can measure and image the elasticity of human tissue. It has been approximately 20 years since elastography been firstly proposed. Various methods

have been devised for estimating tissue elasticity, and these methods combine some forms of tissue excitation technique with certain detection methods.

2.2.1 Static and dynamic excitation methods

Tissue can be either excited statically or dynamically in elastography. In static methods, tissue is compressed and the resultant tissue strain distribution is used to characterize the stiffness, where high stain presents low stiffness and low strain means high stiffness. Difficulty of static methods is to keep the compression uniaxial to ensure the interesting area bears the same force [32]. Moreover, strain distribution can be distorted at boundaries, making the quantitative measurement to be a problem [33]. While in dynamic excitation, elasticity characterisation relies on wave equation, in which distribution of tissue displacement is used to characterize the shear moduli.

2.2.2 External excitation methods

From the aspect of excitation position, elastography techniques can be also categorized into external excitation and internal excitation. External methods use direct mechanical means to apply force on the skin to deform tissue beneath. Internal methods generally use acoustic radiation force (ARF) at the focal region of ultrasound to excite the tissue interests.

One of the approaches for external methods is the low-frequency surface vibration. In [34], a low frequency (10 – 1000 Hz) vibrator directly applied on the tissue surface, which generated a tissue motion that beavered differently as a response to different stiffness. Pulsed Doppler system was used to detect this motion and stiffness variation can be displayed according to the tissue motion. This approach was then improved by using multi-frequency vibrator to allow elasticity imaging with colour Doppler imaging [35-37].

Another major external excitation approach is the step surface displacement, which was firstly reported by Ophir in 1991 [38]. In this method, force is applied to the skin surface for a long time until the tissue motions become steady and the resultant deformation is measured ultrasonically. The force could apply in either a single step or a sequence of incremental steps. Images are taken both before and after compression steps to estimate a dense field of displacement from the difference of two images. Linear displacement change indicates a homogenous tissue, while if a local deviation appears in the linear slope [39], that indicates tissue is heterogeneous. The advantage of this technique is that the ultrasound transducer can be used to produce a localized tissue compression near the region of interest. However disadvantage is the high requirement of uniform tissue compression, in addition the tendency

of objects could move out of image plane after compressions. Thus, many improvements of this method have been made from the study of correlation [40], zero-crossing tracking [41], strain increments [42, 43] and estimation of signal envelopes with two-dimensional window of radio-frequency [44]. Major engineering efforts have also improved the signal processing and systems implementation. In addition, efforts are been made to solve inverse problem and obtain quantitative images [45-47].

2.2.3 Internal excitation methods

Typical example of internal excitation is the use of acoustic radiation force, which is a result of momentum transfer from ultrasound to surrounding tissues due to acoustic absorption and scattering [48]. Sugimoto et al. is probably the first to use ARF for tissue elasticity imaging in 1990 [49]. They used ARF to generate localised deformations in tissue and acqure informations of localised stiffness by fitting tissue displacemnt against time. However it was not until the year of 2002, a technique named acoustic radiation force impulse imaging (ARFI) was devised [50], and since then the AFR method began to be appreciated. In this technique, short-duration acoustic radiation forces were used to generate localized displacements in deep tissue and cross-correlation method was used to track the displacement. Compared with surface displacement elastography, ARFI imaging presents better imaging contrasts [51]. Moreover it has deeper imaging depth because in principle ARF can be excited at anywhere ultrasound focus can reach. However, the disadvantage is that tissue displacement generated by ARF is relative week even with a high intensity focused ultrasound, which limited the signal to noise ratio of this technique [52].

In the other hand, the product of ARF, shear waves, has been studied for elasticity imaging. In 1998, Sarvazyan et al. [17] reported the use of ARF to generate shear waves that propagate perpendicularly and away from ultrasound focus. These shear waves could be detected and the velocity of them can be used to quantitatively estimate the elasticity of tissue. Further to this method, Nightingale et al. [53] measured the shear wave speed point by point by axial translation of the focused beam, from which a two-dimensional image of the Young's modulus fields was constructed. Later on, they developed a time-to-peak lateral displacement estimator as an alternative way to estimate the shear wave speed [54]. In the other hand, Bercoff et al. [55] developed a high speed scanner (10000 imaging frames per second) that had significantly speeded up the monitoring of shear waves generated by ARF impulse within the tissue. In their system, multiple pulses fired at a high rate and the shear wave propagation was tracked by the ultrasound echoes. More recently, a method named spatially modulated

ultrasound radiation force (SMURF) has been devised [56]. They set up a unique spatial frequency within a region of tissue by applying a spatially modulated pattern. By measuring the temporal history of displacements, the local shear wave speed was estimated. This method has been validated on a phantom, as well as an *ex-vivo* porcine liver [57]. In the other hand, the dependence of shear wave on the viscoelasticity of tissue was demonstrated by modelling the propagation of low-frequency shear waves [58]. The viscoelasticity maps are potentially more useful than Young's modulus maps as the elasticity itself has not proved to be completely adequate for tumour characterization.

2.2.4 Detection methods for elastography

Motion of tissue can be detected either ultrasonically or with magnetic resonance imaging (MRI) system, or optically. Ultrasonic detection is widely used because of the low cost and real-time. However, in the track of small displacement ultrasonic system may present poor signal-to-noise ratio. MRI could be an option to overcome this. MRI is more expensive than ultrasound, but it can measure all three spatial components of motions with high precision and thus is more suitable for quantitative elastography. Magnetic resonance elastography (MRE) has shown the possibility in the detection of breast [59] and prostate cancer [60], and the monitoring of invasive therapeutic techniques [61] and characterisation of mechanical properties of brain [62] and plantar [63]. Optical systems have also been applied for a purpose of elastography. Schmitt [64] used a free-space Michelson interferometer to track the speckles induced from the tissue motion to produce compression elastography. Kirpatrick et al.[65] applied the OCT system to track the large and small deformations in tissue. Also, based on excitation by a ring actuator, Kennedy et al. [66] presented a novel sample arm arrangement for dynamic optical coherence elastography. The advantages of optical methods are the incomparable high-resolution as well as the character of real-time.

2.2.5 Limitation in skin characterisation

Although tissue elasticity imagining provides many advantages in medical diagnosis, there are still restrictions in widening the range of applications. For example, current elastography techniques that can provide quantitative elasticity imaging are all based on tracking shear wave speeds. However, shear wave spreads in bulk of tissue and thus can only provide reliable stiffness evaluations for local bulk tissues. This potentially degrades the imaging resolution if we use current elastography techniques to characterise skin elasticity. Compared with this, surface acoustic waves (SAWs) provides advantages in skin characterisation as

SAWs spread on surface and most of the wave energy localised in skin. Therefore inspired by elastography techniques but as an improvement, using SAWs speed instead of shear waves can potentially provide more localised characterisation of skin elasticity. This dissertation aims to develop such a technique.

2.3 Surface acoustic wave generation and detection

2.3.1 Surface acoustic waves

There are three principle modes of acoustic waves in solids, namely are longitudinal waves, shear waves and surface waves, depending on how particles moving in solid during wave propagation. Longitudinal wave, sometimes referred as compressional waves, move in the same direction as solid particle moves. Shear waves, or transverse waves, move in the direction perpendicular to the solid particles movement. When acoustic waves propagate to interface, wave mode conversion happened. At the interface of solid and free space, both of longitudinal and shear waves are converted to surface waves. As a result, particles on the surface involve two essential movements that are coupled with each other: longitudinal oscillations perpendicular to surface and transverse oscillations parallel to surface. Therefore, particle movements induced by SAWs follow an elliptic orbit, and the axis of orbit is perpendicular to the medium surface which is illustrated in the Figure 2- 2.

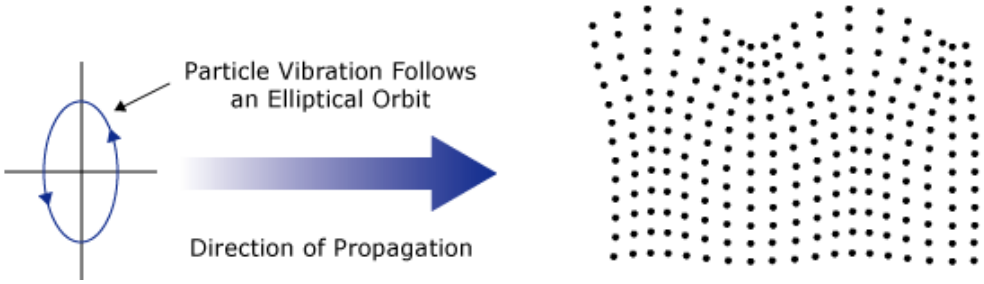

Figure 2- 2 Schematic view of surface acoustic wave and the orbit of particle movement.

One of the important SAWs applications is the SAW devices which are recognized for their versatility and efficiency in controlling and processing electrical signals. Also, SAWs are widely used in non-destructive testing (NDT). By analysing SAWs signal in time and frequency, SAWs can be used to detect the position of any defects and calculate their size. Characterisation of skin by SAWs is actually a transfer and novel application of NDT technique from industry to medical practice.

Surface acoustic waves can be generated and detected in quite a few ways, either by contact mechanisms or non-contact mechanisms. In next section, common-used methods for both SAWs generation and detection methods were reviewed and discussed. Based on this, SAWs generation and detection methods used in our research work were finally decided in the consideration of lab facilities and the advantage and disadvantage of each method.

2.3.2 Surface acoustic wave generation

SAWs generation by mechanical impulses

Surface acoustic waves can be generated either by contact mechanisms or non-contact mechanisms. The most traditional and simplest way is to load a direct mechanical vibration impulse on the surface of sample to act as acceleration and hence excite the surface acoustic waves in such contact manners.

Acoustic waves that are propagating in an isotropic medium with linear elasticity satisfy the following equation:

$$\rho\ddot{U} = (\lambda + 2\mu)\nabla(\nabla \cdot \mathrm{U}) - \mu\nabla \times \nabla \times \mathrm{U} \ , \tag{2- 7}$$

where U is the transient displacement of acoustic waves , and λ and μ are Lame constants of the medium which can be derived from the Poisson's ratio, Young's modulus and density ρ.

Considering a harmonic excitation force perpendicularly acting on the free surface of an isotropic elastic solid in a circular behavior, equation (2-7) has been solved by Miller and Pursey in the cylindrical polar coordinate system [67]. The displacement of acoustic wave can be expressed as

$$U_z = \frac{a}{\mu}\int_0^\infty \frac{\sqrt{\xi^2-1}\,J_1(ak_1\xi)}{R(\xi)}\{2\xi^2\exp\left(-k_1 z\sqrt{\xi^2-\gamma^2}\right) + (\gamma^2-2\xi^2)\exp(-k_1 z\sqrt{\xi^2-1})\}J_0(rk_1\xi)d\xi$$

$$U_r = \frac{a}{\mu}\int_0^\infty \frac{\xi\,J_1(ak_1\xi)}{R(\xi)}\{2\sqrt{\xi^2-\gamma^2}\sqrt{\xi^2-1}\exp\left(-k_1 z\sqrt{\xi^2-\gamma^2}\right) + (\gamma^2-2\xi^2)\exp(-k_1 z\sqrt{\xi^2-1})\}J_1(rk_1\xi)d\xi \tag{2- 8}$$

where a is the radius of circular force stimulus, ξ is the integration variable in wave number domain that is normalised with respect to k_1; $k_1 = \omega\sqrt{\rho/(\lambda+2\mu)}$ and $k_2 = \omega\sqrt{\rho/\mu}$ stand for the longitudinal and shear wave wavenumbers, and ω denotes for the angular frequency of excitation force. J_0 and J_1 refer to the Bessel function of the first kind, and γ is ratio of shear and longitudinal wavenumber.

The term of $R(\xi) = ((\gamma^2 - 2\xi^2)^2 - 4\xi^2\sqrt{\xi^2 - \gamma^2}\sqrt{\xi^2 - 1})$ in equation (2-8) is the well-known Rayleigh function. For surface acoustic waves, the solution of wave displacement fields can be greatly come down to the solution of $R(\xi)$, and only those satisfying $|\xi^2| > |\gamma^2|$ are the true solutions for SAWs displacement.

Exact solutions of the Rayleigh function have been extensively studied in [68-70], and the out of plane displacement and surface following displacement fields of surface acoustic waves can be expressed as follows,

$$U_z(r,t) = \frac{2r_o f(t)}{\pi^2} \times \mathrm{Im} \int_0^{\pi} \frac{r_o - r\cos\theta}{\rho} d\theta \times \int_0^{\frac{\pi}{2}} \frac{\alpha}{c_s^2 R(\varepsilon)} \frac{d\varepsilon}{dt} \cos\varphi \, d\varphi$$

$$U_r(r,t) = \frac{2r_o f(t)}{\pi^2} \times \mathrm{Re} \int_0^{\pi} \cos\theta \, d\theta \times \int_0^{\frac{\pi}{2}} \frac{\varepsilon(\varepsilon^2+\beta^2) - 2\varepsilon\alpha\beta}{R(\varepsilon)} \frac{d\varepsilon}{dt} \, d\varphi \quad (2\text{-}9)$$

where $R(\varepsilon) = (\varepsilon^2 + \beta^2)^2 - 4\varepsilon^2\alpha\beta$ is another expression form of the Rayleigh equation, in which $\alpha = \sqrt{\varepsilon^2 + 1/c_l^2}$, $\beta = \sqrt{\varepsilon^2 + 1/c_s^2}$, $\varepsilon = i(1/\sigma\cos\varphi)$, $\sigma = \sqrt{a^2 + r^2 - 2ar\cos\theta}$, and C_s and C_l denote for the phase velocity of shear wave and longitudinal wave in the sample.

Even though SAWs generation by mechanical impulses is a relative simple and easy-achieved way (for example, an electro-magnet shaker could be a good applicator which is in low cost), there are still quite a few limitations induced by the contact generation mechanism. For example, the contact extent can heavily influence the quality of generated surface acoustic waves.

SAWs generation by Snell's law

As described previously, acoustic waves can travel in various modes in solid, namely are longitudinal waves, shear waves and surface waves. One of the wave modes can transfer to another when acoustic waves penetrating through an interface. This mode conversion is due to wave refraction at interface, and it happens only if acoustic wave is incident with an angle. For example, when longitudinal wave penetrating though an interface obliquely, part of wave energy generate particle movement in transverse direction and hence induce refracted transverse (shear) waves. Rest of wave energy will transfer to the refracted longitudinal waves. Acoustic wave mode conversion is described in the Figure 2-3 and it follows the well-known Snell's law:

$$\frac{\sin\theta_1}{V_{L1}} = \frac{\sin\theta_2}{V_{L2}} = \frac{\sin\theta_3}{V_{S1}} = \frac{\sin\theta_4}{V_{S2}}, \quad (2\text{-}10)$$

where V_{L1} is the velocity of incident longitudinal wave in material 1 and $\boldsymbol{\theta_1}$ is the incident angle; V_{L2} is the velocity of refracted longitudinal wave in material 2 and $\boldsymbol{\theta_2}$ is the refracted angle for $\boldsymbol{L_2}$; V_{S1} is the velocity of converted shear wave in material 1 and $\boldsymbol{\theta_3}$ is the reflected angle for $\boldsymbol{S_1}$, and V_{S2} is the velocity of refracted shear wave in material 2 and $\boldsymbol{\theta_4}$ is the refracted angle for $\boldsymbol{S_2}$.

In the case of that acoustic waves propagate from a slower to faster material, one can find an incident angle making the refractive angle θ_2 and θ_4 to be 90°. When θ_2 reaches 90°, the refracted longitudinal wave L_2 is converted to a surface following longitudinal wave, sometimes also referred as creep waves. At this time, incident angle θ_1 is called the first critical angle. Creep waves are actually the longitudinal component of surface acoustic waves. However, as it decays very fast, the surface following mode is difficult to find any application in practice. Beyond the first critical angle, incident longitudinal waves will all convert to refracted shear waves travelling in the medium 2.

When θ_4 reaches 90°, the incident angle θ_1 is called the second critical angle. At this angle, entire refracted shear wave S_2 will convert to surface following shear waves, and all the incident wave L_1 will convert to surface acoustic waves if the incident angle beyond the second critical angle. This is basically the principle of how to generate surface acoustic waves by Snell's law, and in reality, people normally realize this by using an ultrasonic edge-transducer. Figure 2-4 describes the typical structure of ultrasonic edge-transducers.

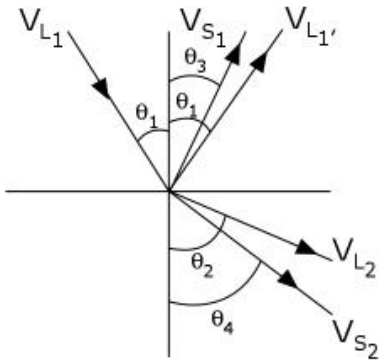

Figure 2-3 Refraction of acoustic waves cause the acoustic mode conversion [71]

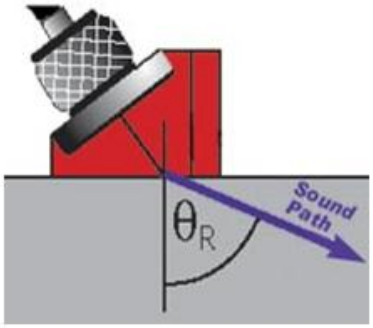

Figure 2-4 Typical structure of an edge ultrasonic transducer [71]

The edge-transducer consists of two parts: a normal piezo-electric ultrasonic transducer probe (grey) to generate incident longitudinal waves, and a couplant-material in edge-shape (red) to allow the wave mode conversion by making an acoustic incident angle. From Snell's law, one will get the equation below at the second critical angle,

$$\sin\theta_1 = \frac{V_{L1}}{V_{S2}}, \tag{2- 11}$$

and we will find the second critical angle exists only if the longitudinal wave velocity in edge ($\mathbf{V_{L1}}$) is lower than the shear wave velocity in specimen ($\boldsymbol{V_{S2}}$). However, shear wave speed in biological soft tissues is typically a few m/s, which is much slower compared with 1500 m/s, the sound speed in water, which is usually used as the ultrasound couplant in practice. Therefore, SAWs generation by mode conversion is impossible in biological tissues, and this method is usually used for metallic materials in which shear wave speed is much faster.

SAWs generation by EMAT

EMAT stands for electromagnetic acoustic transducer which offers a non-contact means for generation and detection of ultrasound in electro-conductive materials or magnetic samples. Figure 2-5 depicts the working principle of EMAT for generation of surface acoustic waves.

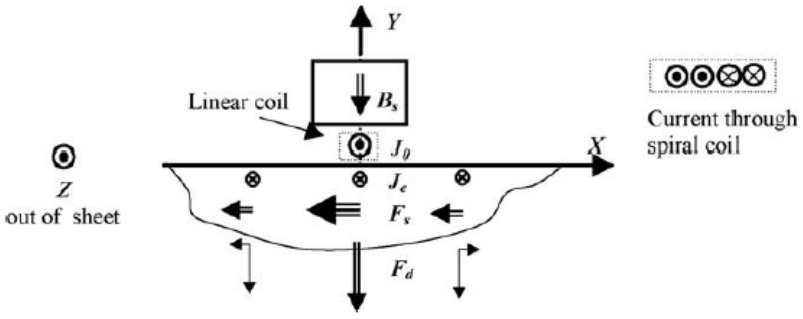

Figure 2-5 Working principle of EMAT for the generation of SAWs [72]. Bs is static magnetic field, Jo is the excitation current, J_1 is the eddy current, and F_d and F_s are the Lorentz forces induced from the dynamic and static magnetic fields.

Core structure in EMAT is coil. When dynamic current passes through the coil, electromagnetic waves will be emitted from the coil and induce eddy current within the near-surface region of sample. Meantime, a dynamic magnetic field is introduced by the EMAT coil and interacts with the eddy current at sample surface following the Lorentz principle. Consequently, Lorentz forces are generated, which act perpendicular to the sample surface and trying to move sample apart from the coil. If an external static magnetic field is also in presence, a supplementary Lorentz force contribution will be added on. The Lorentz forces will eventually excite surface acoustic waves [73-75].

Laser generation of SAWs

SAWs generation by laser is a series of energy conversion. When laser pulses illuminate on tissue, partial laser energy will be absorbed and cause a rapid localised heating. As a result, sample suffers a rapid thermal expansion which in turn excites the acoustic waves. Therefore, laser generation of acoustic waves can be summarised as two procedures: transfer of electro-magnetic energy (laser) to thermal energy (heating), and conversion of thermal energy to mechanical energy (acoustic waves).

If laser power is sufficient low, whole procedure follows the thermal elastic regime without any tissue damage (Figure 2-6 a). While if high intensity laser pulses are used, melting and plasma formation could be induced by overheating, and acoustic waves are generated in ablative regime (Figure 2-6 b). Ablative regime sometimes is useful in therapy but not expected in tissue characterisation. Therefore SAWs should be generated in thermal elastic regime for the application of mechanical characterisation of skin.

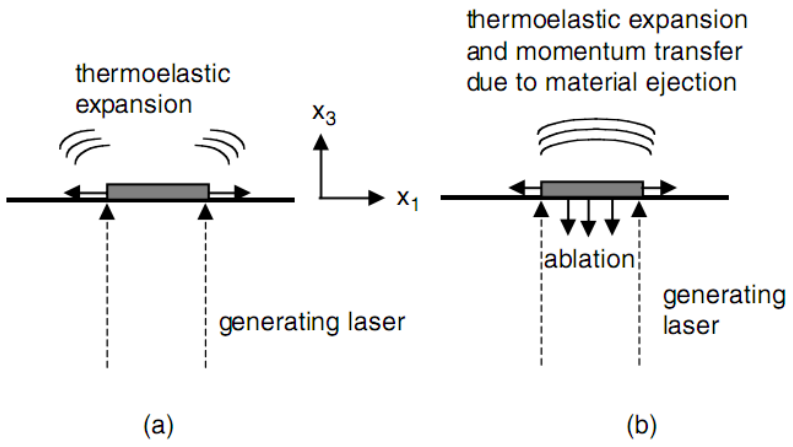

Figure 2-6 Laser generation of acoustic waves in thermo-elastic regime (a) and ablative regime (b) [76]

In thermal elastic regime, the temperature field induced by laser heating is governed by the thermal conduction equation as below [82],

$$k\nabla^2 T(r,z,t) = \rho c\dot{T}(r,z,t) + T_0\beta\nabla\cdot\dot{U} - Q(r,z,t)\,, \qquad (2\text{-}12)$$

where $T(r,z,t)$ is the transient temperature distribution; ρ, c, k represent the density, specific heat and thermal conductivity of the material, and $Q(r,z,t)$ stands for the transient heating source, here, the absorption of laser energy in tissue. Note that acoustic (mechanical) wave damping in tissue can also contribute to tissue heating which is given by the term $T_0\beta\nabla\cdot\dot{U}$ in equation. Since the heat induced by acoustic wave damping is much less than the heat induced by laser, term $T_0\beta\nabla\cdot\dot{U}$ can be neglected in the thermal elastic regime. As a result, thermal conducted equation above can come down to [82]

$$k\nabla^2 T(r,z,t) = \rho c\dot{T}(r,z,t) - Q(r,z,t)\,, \qquad (2\text{-}13)$$

with an simplification to uncoupled thermal-mechanical analysis.

Governed by the thermal conduction equation, tissue suffers a rapid and localized heating during laser exposure. This will cause a large thermal gradient between the heated and surrounding unheated area, resulting in a thermal expansion which in turn excites tissue and generates acoustic waves. In isotropic media, transient displacement of this thermal-elastically generated acoustic wave satisfies the equation below [82]

$$\rho\ddot{U}(r,z,t) = (\lambda+2\mu)\nabla\big(\nabla\cdot U(r,z,t)\big) - \mu\nabla\times\nabla\times U(r,z,t) - \alpha(3\lambda+2\mu)\nabla T(r,z,t)\,, \qquad (2\text{-}14)$$

where $U(r,z,t)$ is the time dependent acoustic displacement field, λ, μ are Lame constants which can be derived from Poisson's ratio, Young's modulus and density ρ of media. α represents the thermal expansion coefficient of sample.

Laser generation of SAWs is a non-contact method, which can eliminate the error induced by variable contact conditions and is applicable to the samples with irregular geometry such as human tissue. In addition, laser generated SAWs are broadband, which potentially give a more localised tissue characterisation at surface [13].

2.3.3 Surface acoustic wave detection

There are four detection modalities reviewed in this section, including piezo-electric transducer (contact), Fibre Bragg grating (optical, contact), wavefront integration

interferometer (optical, contact), and Michelson surface displacement interferometer (optical, non-contact).

SAWs detection by piezoelectric transducer

Physical principle of piezoelectric transducer is the conversion of electrical signals to mechanical vibrations in acoustic generation or the conversion of mechanical vibrations to electrical signals in acoustic detection). Typical transducer consists of five components: piezoelectric element, electrical connections, backing material, transducer housing and the matching layer which are shown in the Figure 2-7.

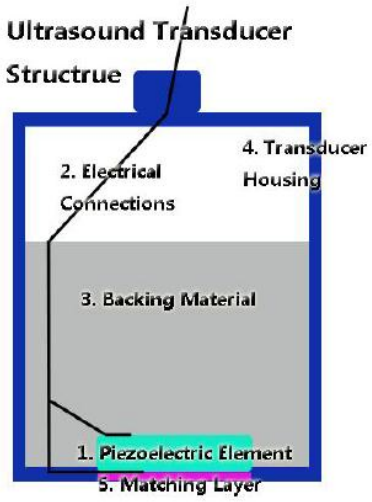

Figure 2-7 Basic structures of piezo-electric transducer

Piezoelectric element is the core of transducer as it conducts the energy conversion between mechanical and electrical energies. Piezoelectric element is selected from polarized materials in which part of molecules is positively charged and the rest are negatively charged when they are connected to an electric field attached to its both sides. The polarized molecules will align themselves with the electric field, resulting in induced dipoles within the molecular or crystal structure of the material. This alignment of molecules causes material to be changed in dimensions. This phenomenon is known as electrostriction, which is the principle of ultrasound generation (Figure 2-8 a). Also, a permanently-polarized material such as quartz (SiO2) or barium titanate (BaTiO3) can produce an electric field when material changes in dimension as a response of external mechanical vibrations. This phenomenon is known as the piezoelectric effect, which is the principle for ultrasound detection (Figure 2-8 b) [71].

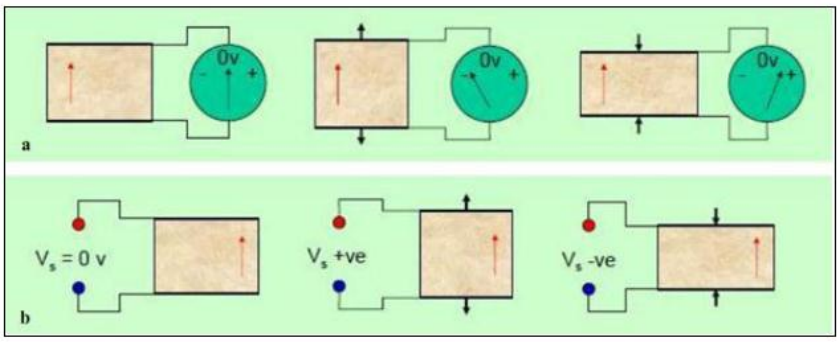

Figure 2- 8 Piezoelectric effect and Electrostriction effect.

Each piezoelectric element has its own resonant vibration frequency depending on the shape and size of element, hence ultrasound transducers work as resonant system and the typical central frequency is MHz with a sideband no more than several KHz. Therefore, for low frequency acoustic waves, for example up to several KHz broadband SAW requires in our system, those ultrasound imaging transducer may not suitable for both generation and detection. In addition, transducer needs to be contact with target and using couplant to match acoustic impedance in detection, which can potentially affect the SAWs propagation. Moreover, the dimension of ultrasound probe is relatively large (compared with optical detection), which may limit the detection resolution to a few millimetres. Therefore, compared with ultrasound transducer, optical detection has quite a few advantages, namely are high resolution, broadband detection, fast scanning and/or non-contact detection. Following is a review of selected optical detection methods.

Fibre Bragg grating

Fibre Bragg gratings (FBG) are made of a fibre core that is fabricated with periodic variations in refractive index, as shown in Figure 2-9. As a contact detection system, Fibre Bragg gratings are required to be bonded or embedded in the sample and the detection of acoustic waves is based on the decoding of the reflectivity spectrum change. When acoustic waves pass through, acoustic strain field modifies the spatial distribution and effective refractive index of FBG. As a result of this, the spectrum of reflectivity will be shifted, and the variation is proportional to the acoustic strain field and also modulated at the same frequency with the acoustic waves as shown in the Figure 2-9 (B). FBGs are generally used as point-to-point scanning sensors as the spatial period of FBG is much smaller compared with the acoustic

wavelength being measured. Drawbacks of FBGs are the limitations in temporal bandwidth due to the radial resonances in optical fibre, and they are normally used to measure the in-plane strains along axis but not suitable for surface acoustic wave detection [77].

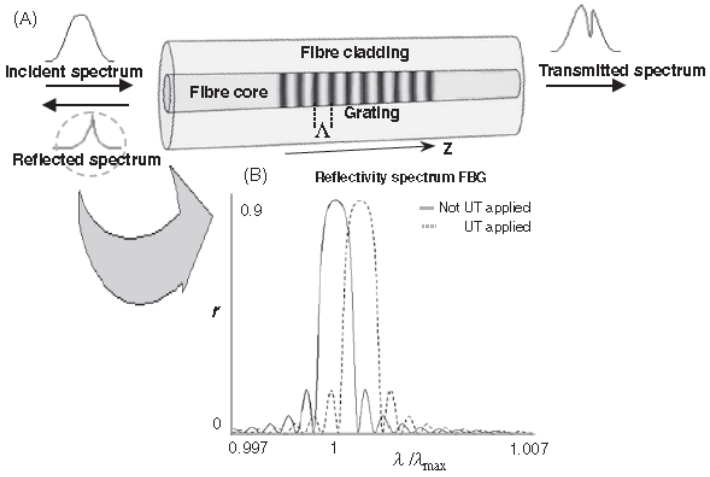

Figure 2-9 Working principle of Fibre Bragg grating. [77]

Wave front integration interferometer

Similar with FBGs, acoustic wave detection with wavefront integration interferometer is also using an optical fibre that is bonded or embedded in the sample as shown in Figure 2- 10 (A). The pressure field of acoustic waves will act on the fibre and hence change the refractive index, resulting in a phase change of the light running through the optical fibre. Therefore acoustic wave detection by wave front integration interferometer is based on the measurement of optical phase modulation. Wave front integration interferometer is named after the fact that lights running through the optic fibre are modulated by a certain portion of the acoustic wavefront rather than by single point of that [77]. Therefore, larger area can be covered in the scanning, making detection much faster than that of point-to-point FBG scanning system. However, main problem of this technique is the complexity of wavefront analysis, which requires the evaluation of both acoustic wavelength and the distance and angle between wave source and wave sensor [77].

Michelson surface displacement interferometer

Michelson interferometer is a point-to-point scanning sensor (Figure 2- 10 B). The acoustic field out-of-plane displacements change the optical path of light in the interferometry sensing arm, as it is reflected from the surface of the sample. This system requires a highly reflective surface and the use of short focal Graded Refractive Index (GRIN) lenses can improve its

sensitivity through effective re-collection of the scattered light. The interferometer demodulates this phase shift to a visible change in optical intensity when the light from the sensor is combined with that from a reference arm, which includes some components (polarization controller, variable attenuator and phase controller) in order to improve the sensitivity of the system by optimising the interferometer performance.

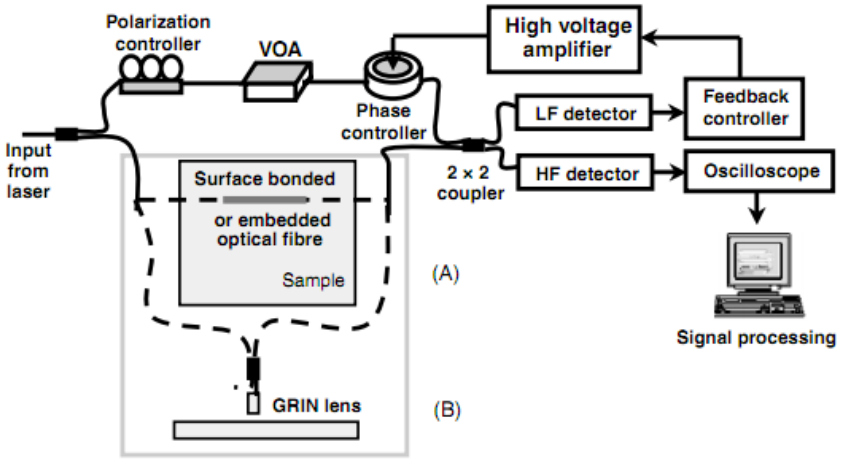

Figure 2- 10 Interferometric system as optical detection of ultrasound: wavefront integration technique interferometer (A), Michelson surface displacement interferometer (B) [77].

Laser vibrometer system

Laser vibrometer is a scientific instrument which measures surface vibration by measuring the frequency (or phase) difference between an internal reference beam and an objective beam. The objective beam is directed to target, and the reflected/scattered beam from target is collected and interfered with the reference beam on a photodetector, typically a CCD array or simply a photodiode. An advantage of laser vibormeter over the conventional interferometry system is that most commercial vibrometers work in heterodyne regime to increase the signal to noise ratio, in which acousto-optic modulator (AOM) or Bragg cell are used to add a known frequency shift (typically 30–40 MHz) to one of the beams. Figure 2- 11 describes a basic structure of laser vibrometer [85].

A beam splitter is used to divide the original laser beam, at frequency f_o, to an objective beam and a reference beam. The objective beam is directed into Bragg cell, though which the frequency is modulated to f_o+f_b. Then the frequency-shifted objective beam goes to target surface hence another Doppler (frequency) shift f_d is added due to the optical modulation by surface vibration. This target motion induced frequency shift can be described by $f_d =$

$2v(t)\cos(\alpha)/\lambda$, where $v(t)$ is the velocity of surface motion as a function of time, α is the laser incident angle, and λ is laser wavelength. As a result, the objective beam is frequency shifted to $f_o + f_b + f_d$ and combined with reference beam in photo-detector, and the interference between two beams leads to a beat frequency at $f_b + f_d$. Since the frequency of original laser beam is very high (> 10^{14} Hz) which is higher than the response of detector, the detector can only detect and respond to the beat frequency at $f_b + f_d$ which is typically in the tens of MHz range. Then by counting the moving interference fringe pattern, displacement and velocity of the surface vibration can be decoded [85].

Advantages of Laser vibrometer include non-contact detection, absolute displacement measurement and high spatial resolution. These advantages are particular important for the real clinical practice. Therefore laser vibrometer was finally chosen to detect the SAWs in our experiment.

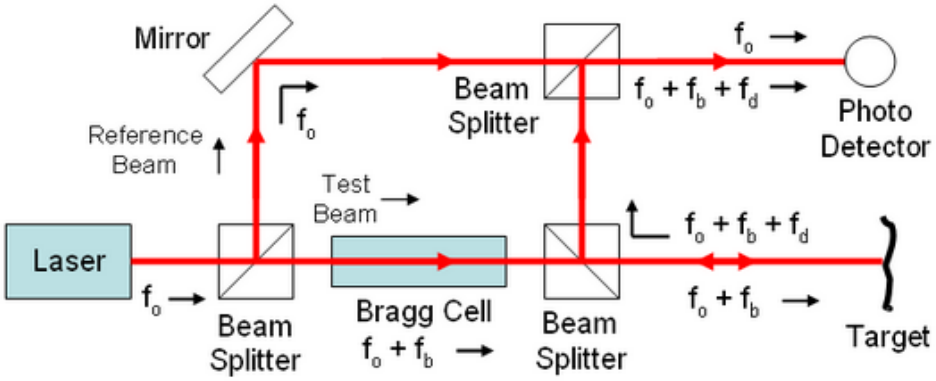

Figure 2- 11 Basic structure of laser vibrometer system

In this chapter, key knowledge of elasticity of soft tissue was introduced firstly, including introduction of different elasticity modulus and their relationship with acoustic wave speeds in biological tissue. Young's modulus was chosen to describe elasticity property in this dissertation. Then a critical review of current modalities for elasticity measurement was given, from which limitations in skin characterisation by using traditional elastography techniques can be seen, and SAWs are proposed to address this limitation. Accordingly, knowledge of SAWs was introduced, more importantly, methods of SAWs generation and detection were reviewed later, providing good references for experimental set-up established in the dissertation. Next chapter is a simulation study of tissue characterisation using surface acoustic waves, from which the feasibility of this technique can be predicted before any experimental investigation.

Chapter 3 FE simulation of tissue characterisation by SAWs

Introduction

In this chapter, theoretical study of mechanical characterisation of tissue using SAWs was investigated by finite element method (FEM). Model consists of two parts: the surrounding soft tissues and a cylindrical piece of stiff inclusion at the surface to mimicking abnormal tissue. SAWs were generated by laser in thermal elastic regime as laser generation has a number of advantages for real clinical practice, such as non-contact, broadband acoustic generation, and easy operation for hard-to-access locations (flexible light delivery using fibre) etc. Out-of-plane displacement of simulated surface vibration was recorded as SAWs signals, and group velocity and phase velocity of SAWs were calculated to characterise the model mechanical properties. In the following, introduction of FEM is given firstly, together with a brief introduction of ANSYS, a commercial FE simulation package used in this dissertation. Then the model creation and meshing scheme were described, following with description of governing equation and boundary conditions in simulation. At last, the simulated SAWs were analysed in both time domain and frequency domain to sense the stiffness variation in both lateral and vertical direction.

3.1 Finite element method

3.1.1 Finite element method

Finite element method (FEM), also known as finite element analysis (FEA) for its practical application, is a numerical method to get approximation solutions by solving partial differential equations (PDE) as well as integral equations. For steady state solutions, approaches of FEM are made by solving the partial differential equations completely. While for dynamic solutions, PDE are always rendered into an approximated system of ordinary differential equations (ODE) and then solutions are numerically integrated using standard techniques such as Euler's method, etc.

FEM provides good mathematical approximation to solve engineering problems with complex geometries and domains which are not easy to address with classical numerical analytical methods, and FEM has been developed into an indispensable technique for simulating various engineering problems by solving thermal, fluids, structure, electro-magnetic and their multi-physical fields. Many commercial software packages, such as ANSYS, ABAQUS and COMSOL, are developed for a convenient implementation of FEM

simulation in scientific researches. Here we choose ANSYS for its high reputation in linear solver and its high performance in thermal-structure coupling analysis.

3.1.2 Introduction of ANSYS

ANSYS is a large-scaled general FEA package providing resolutions for many physical fields. The built-in physics interfaces make it possible to build models by simply defining relevant physical quantities such as material properties, loads, constraints, sources, and fluxes. These variables, expressions, or numbers could be directly applied to domains, boundaries, edges, and points independently of the computational mesh, and then the software itself internally compiles a set of equations to represent the entire model. In ANSYS, conventional models can be extended from one type of physics into multi-physics, so that coupled-physics fields can be analysed and solved simultaneously. In addition, ANSYS provides strong data sharing functions to allow data exchange with other computer aided design (CAD) software such as AutoCAD, Solidworks and Pro/Engineer.

In practice, ANSYS contains three processors: pre-processor, processor and post-processor which are typically used in sequence in an operation. The pre-processor provides powerful tools to create a model and then mesh it to be adaptive for FEM in ANSYS. In processor, various numerical solvers are provided for different analysis to give solution of partial deferential equations following the basis of laws of science using FEM. Then, solutions can be outputted or presented in different formats with various signal processing operators in post-processor. For example, one can plot the contour mapping, gradient field, time history, or path mapping of either a single component or the entire vector of an argument.

3.2 Simulation of laser generation of SAWs

3.2.1 Model creation

In ANSYS, models can be created either in a way of ‘top to down’, in which users define the highest-order graphics primitives (such as sphere and block) and the program automatically generates the relevant lower-order graphics primitive (e.g. area, line, key point), or, oppositely, in a way of ‘down to top’, in which users define each low-order graphics primitives and the program assembles them up to a higher-order graphic primitive. Besides, users can also use Boolean operation (e.g. add, subtract, glue, overlap, etc.) to make up these graphic primitives, so that a solid model can be created in a way of ‘sculpture’.

Model used in our simulation is schematised in the Figure 3- 1. A symmetric 2-D model was created to save the computing time, axisymmetric to x axis. The model contains two parts, a cylindrical (square in 2D)stiff region to represent the diseased tissue and a concave ambient soft region to simulate the surrounding normal tissues. Therefore the stiffness of model changes in both x axis, from soft to hard and to soft again along model surface, and in y axis, from hard to soft at the stiff region.

Model was created in a way of 'top to down', which means the square and concave shape (high-order graphics primitives) were defined by user and the lines and key points (low-order graphics primitives) were generated automatically by the program. However, the model created in this way generates two borderlines overlapped with each other at the boundary (red in figure); one is belong to the square graphic primitive and the other is belong to the concave graphic primitive. In order to make them to be able to 'talk' or 'interact' with each other, for example, allowing thermal diffusion and wave propagation from one to the other, two parts were operated with 'glue' function so that the two graphic primitives become to share one borderline at the interface and thus became connected with each other.

Dimension of model can be seen from the figure 3-1, and the thermal and elastic properties of two parts were specified in the Table 3- 1 to allow the simulation of thermal-elastic analysis. In Table 3- 1, the thermal parameters cited the values of skin from [78], and we assumed that thermal parameters are independent of slight stiffness change so that the thermal parameters were specified as the same for soft and hard tissues in the model. Young's modulus of hard tissue were specified about 6 times bigger than soft, and the order of magnitude cited the elastic measurement of TMM phantoms in [14].

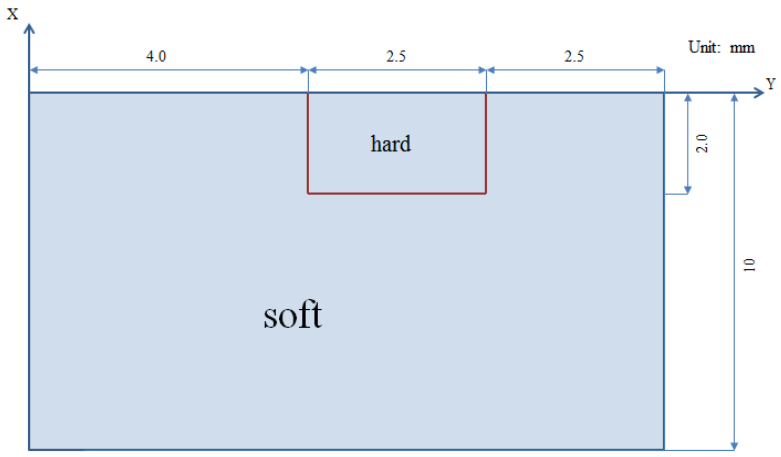

Figure 3- 1 Schematic of model in ANSYS

Table 3- 1 Thermal and elastic properties of finite element model

Parameters	Soft tissue	Harder soft tissue
Density (kg/m^3)	1060	1080
Specific heat (J/kg·K)	3300	3300
Thermal expansion coefficient (K^{-1})	3e-4	3e-4
Thermal conductivity (W/m·K)	0.45	0.45
Young's Modulus (Pa)	87097	511147
Poisson's Ratio	0.49	0.49

3.2.2 Model mesh

Model needs to be divided into certain grids to allow the solution of partial differential equation and integration in the finite element method. ANSYS provides high quality meshing functions, and there are four methods available for a rapid generation of finite element grids.

Mapping-mesh allows user to divide the whole geometry to several relatively regular parts and then mesh each individual parts by generation of mapping-grids with proper element property and grids control. The grids generated in mapping-mesh are in high regularity, and hence can enhance the accuracy of solution. Mapping-mesh is particular suitable for a model with simple geometry, and on the contrary, it is not proper to use for a model with complex geometry since mismatch of grids can be generated when resembling the already-meshed individual parts as a whole. To compensate this, the free-meshing mode is much more easy-to-use for meshing a model with a pretty much complex geometry. With powerful function of free-meshing program, one can mesh a complex model in direct and the program will generate proper element control (e.g. change in element size and shape) to make the elements to be adaptive to the complex geometry boundaries. The third mode is the adaptive-mesh, in which boundary conditions are already loaded on the model before meshing, and users indicate program to automatically generate a pre-grids and then analyse and estimate the discretization error of the grids subject to the boundary conditions. Based on the error estimated, program re-defines the grids and then analyses and estimates the grids discretization error again, and it repeats this cycle until the discretization error converges to a user-defined value or the program has reached a user-defined repetition times. The aim of adaptive-mesh is to achieve a good compromise between the time-consuming of computation and the accuracy of solution. The last mode, extension-mesh, can extend a 2-D grids to 3-D

in convenience. For example, for meshing a cylindrical modal, one can either mesh the bottom area (circle) and then extend it along the axis to form a cylinder, or mesh a half longitudinal section and then rotates it along axis to the cylinder. In summary, different meshing modes have their unique advantages and application. One needs to choose the meshing methods carefully according to the specific needs of a model.

Our model was meshed in the mode of mapping-mesh because the geometry of model is simple and regular and so the mapping-mesh can generate elements in higher regularity. The elements shape was specified as quadrangle and the dimensions of grids were decided according to the New Mark's scheme as shown below,

$$L_e = \frac{l_{min}}{20}, \tag{3- 1}$$

where L_e is the size of element, l_{min} stands for the minimum length of interest, here, the minimum wavelength of laser generated surface acoustic waves which is the product of surface acoustic wave velocity and the reciprocal of maximum frequency of surface acoustic wave generated in the model.

The maximum frequency of the surface acoustic waves generated by a pulsed laser with a Gaussian spatial profile and temporal distribution of Dirac Function can be described by the following equation[79]:

$$f_{max} = \frac{\sqrt{2}C_R}{\pi R_0}, \tag{3- 2}$$

where R_0 is the width of the Gaussian distribution, thus the minimum wavelength is evaluated as

$$l_{min} = \frac{\pi R_0}{\sqrt{2}}, \tag{3- 3}$$

In the simulation, the laser radius is assumed as 0.5 *mm* and so the l_{min} is estimated as 0.9 *mm*. Then the element size is decided as 45 μm following the New Mark's scheme described by the equation 3-3.

As it is known, penetration of surface acoustic waves is comparable to wavelength, that is to say, high frequencies (short acoustic wavelength) concentrated in the near-surface region and only those low frequencies (longer acoustic wavelength) can reach at deep depth. Therefore the estimated element size, 45 μm, needs to be refined to save the computing resource.

Whole model was divided into 16 sections (shown in Figure 3- 2) and meshed with different grids size according to the different acoustic wavelength reaches at different depth. In the

near-surface areas, the element size was increased from 10 μm (for those who are within/close to laser source) to 20 μm (for those who are apart from laser source), all slightly smaller than 45 μm for safety margin to ensure the calculation accuracy. In addition, along the depth direction, the element size increases gradually and the details of the grids size in each section can be seen from the modelling code which is attached in the Appendix.

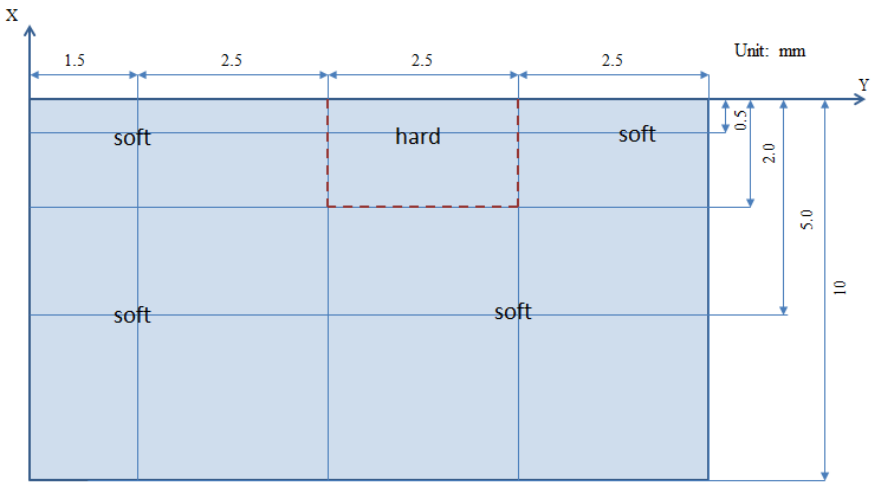

Figure 3- 2 Model was divided into 16 sections to refine the grids size

The material properties in table 3 were loaded into the elements in soft and hard region respectively, and the element type was specified as PLANE-55 in thermal analysis and PLANE-42 in the subsequent thermal-elastic mechanical analysis to complete the assignment of element property. Below is a brief introduction of the two element types in ANSYS.

PLANE 55 can be used as a plane element or as an axisymmetric ring element with a 2-D thermal conduction capability. The element has four nodes with a single degree of freedom, temperature, at each node. Therefore the element is applicable to a 2-D, steady-state or transient thermal analysis. If the analysis contains thermal-elastic analysis, the temperature element can be replaced by an equivalent structural element, such as PLANE 42 which is used for 2-D modelling of solid structures. PLANE 42 can be used either as a plane element (plane stress or plane strain) or as an axisymmetric element. The element is defined by four nodes having two degrees of freedom at each node: translations in the nodal x and y directions. The element has plasticity, creep, swelling, stress stiffening, large deflection, and large strain capabilities.

3.2.3 Governing equation

In FEA, the thermal conduction equation can be re-formulated as [83]

$$[K]\{T\} + [C]\{\dot{T}\} = \{Q\}, \quad (3\text{-}4)$$

where $\{T\}$ is the temperature vector, $[K]$ and $[C]$ are the thermal conductivity and heat capacity matrix, and $\{Q\}$ is the heat source vector. Accordingly, the displacement fields induced by the thermal expansion can be expressed as below, without taking consideration of viscosity damping [83]:

$$[M]\{\ddot{U}\} + [S]\{U\} = \{F\}, \quad (3\text{-}5)$$

$\{U\}$ stands for the displacement vector, and $[M]$ and $[S]$ are, the mass matrix and stiffness matrix of tissue respectively. The term $\{F\}$ is the force source vector which is coupled to the thermal expansion as [83]

$$\{F\} = \int [B]^T [D]\{\varepsilon_0\} dV, \quad (3\text{-}6)$$

where $[B]^T$ is the transpose of derivative of the shape function, $[D]$ is the material matrix, $\{\varepsilon_0\}$is the thermal-strain vector and V stands for the volume of an element.

3.3 Boundary conditions

In analytical analysis, governing equations control the whole physical process and the boundary conditions define loads and constrains in a model which will probably determine the final physical effects. In the modelling of thermal-elastic problem, both of thermal and mechanical boundary conditions need to be specified.

3.3.1 Thermal boundary conditions

When a laser pulse incident on the sample, it normally uses the second boundary conditions - the heat flux of a laser beam to describe the thermal boundary conditions. The heat generated by the laser pulse is input as a surface heat flux and can be described by the following expression [84]:

$$-k \frac{\partial T(r,z,t)}{\partial z} \Big|_{z=o} = A * I_0 f(r) g(t) h(z), \quad (3\text{-}7)$$

and

$$\frac{\partial T(r,z,t)}{\partial z} \Big|_{z=h} = 0, \quad (3\text{-}8)$$

where A is the optical absorption coefficient of tissue, I_0 is the laser irradiance which is described by the laser pulse power per unit area, so that the term $A * I_0$ describes the density of laser power that is actually delivered to the tissue. $f(r,z)$ and $g(t)$ are the spatial and

temporal profile of laser. In addition, *h(z)* describes the laser attenuation and scattering behaviour within tissue. *k* is the thermal conductivity of tissue and *h* is the thickness of tissue.

The laser irradiance can be calculated by [78]

$$I_0 = \frac{2W}{\pi r_0^2 t_0}, \tag{3- 9}$$

in which *W* is the laser energy, t_0 is the rise time of a laser pulse, and r_0 is the laser radius.

There are many spatial modes in laser devices and the Transverse Electromagnetic Mode (TEM) is the most common-used one. Here we choose TEM00 as an example to apply in the modelling configuration as it is the most fundamental among various TEM laser devices. Laser beams emitted from this mode are distributed in Gaussian Profile, which can be described by [78]

$$f(r) = \exp\left(\frac{-r^2}{r_0^2}\right), \tag{3- 10}$$

, term *r* represents the radius coordinate that is perpendicular to the laser incident direction.

Figure 3- 3 is a schematic of laser radiation in Gaussian shape, the peak value locates at central point and the optical radiation gradually fades out toward both sides.

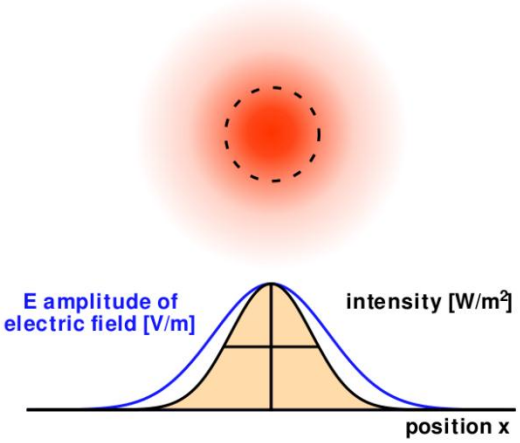

Figure 3- 3 Schematic of the electro-magnetic fields of a laser beam in a Gauss spatial mode

There are also several temporal modes available for a laser device; typical ones include the pulses mode, the q-switched mode and the mode-locked mode. In the modelling set-up, a laser source in Gaussian temporal profile was employed because of its representativeness in the practice, and the temporal profile can be described as [78]

$$g(t) = \left(\frac{t}{t_0}\right) \exp\left(-\frac{t}{t_0}\right), \tag{3- 11}$$

where t_0 is the rise time of laser pulse.

When a laser pulse is incident on tissue, laser energy diffuses considerably in depth due to the optical absorption and scattering within tissue. The optical diffusion largely depends on the laser parameters, which can be described by [78 84]:

$$I_d = I_0 \exp\left(-\sqrt{3\mu_a}\left(\mu_a + \mu_s(1-g)\right)z\right), \quad (3\text{- }12)$$

where I_0 is the laser irradiance, I_d is the irradiance of laser that actually reaches to the depth z after diffusion, μ_a and μ_s are the optical absorption and optical scattering coefficient respectively, and g is the scattering anisotropy, leading to a reduced scattering coefficient. Relevant parameters of different laser devices can be seen from the Table 3- 2, and the Nd: YAG 532 nm was used in the modelling configuration.

Therefore, the thermal boundary conditions applied in the modelling can be described as following as a whole:

$$-k\frac{\partial T(r,z,t)}{\partial z} = \mu_a \cdot \frac{2W}{\pi r_0^2 t_0} \cdot \exp\left(\frac{-r^2}{r_0^2}\right) \cdot \left(\frac{t}{t_0}\right) \exp\left(-\frac{t}{t_0}\right) \cdot \exp\left(-\sqrt{3\mu_a}\left(\mu_a + \mu_s(1-g)\right)z\right), \quad (3\text{- }13)$$

3.3.2 Mechanical boundary conditions

In the thermal expansion analysis, the temperature fields solved from thermal analysis were input as a load, and it can be described as [83]

$$n \cdot [\sigma - (3\lambda + 2\mu)\alpha T(r,z,t)I] = 0, \quad (3\text{- }14)$$

where $\boldsymbol{T}(\mathrm{r},\mathrm{z},\mathrm{t})$ is the thermal field induced by laser pulse, n is the unit vector that is perpendicular to model surface, I is the unit tensor, σ is the stress tensor, and λ and μ are the lamb constant of tissue sample.

Mechanical boundary-conditions which are needed to be specified in order to constrain the thermal-expansion process, are showing as below [78]:

$$\mathrm{U}(\mathrm{r},\mathrm{z},\mathrm{t})\Big|_{\mathrm{t}=0} = \frac{\partial \mathrm{U}(\mathrm{r},\mathrm{z},\mathrm{t})}{\partial \mathrm{t}}, \quad (3\text{- }15)$$

and

$$\mathrm{U}(\mathrm{r},\mathrm{z},\mathrm{t})\Big|_{\mathrm{z}=\mathrm{h}} = \frac{\partial \mathrm{U}(\mathrm{r},\mathrm{z},\mathrm{t})}{\partial \mathrm{t}}, \quad (3\text{- }16)$$

, in which the $\mathrm{U}(\mathrm{r},\mathrm{z},\mathrm{t})$ stands for the displacement of tissue particles, and the whole equation means there is no oscillation introduced on the tissue surface at the initial time, and bottom of

tissue are fixed all through the modelling time so that the displacement of bottom boundary is constrained as zero.

Table 3- 2 Optical parameters of different lasers in tissue [78]

Laser	Wavelength	μ_a ($mm^{-1)}$	μ_s (mm^{-1})	g	Penetration depth (mm)
CO_2	10600	82	-	0.9	0.012
Er:YAG	2960	1000	-	0.9	0.01
Laser Diode	1540	1.0	1.1	0.9	0.40
Laser Diode	1450	1.6	1.2	0.9	0.27
Nd: YAG	1320	0.1	0.14	0.9	1.49
Nd: YAG	1064	0.01	0.3	0.9	10
Laser Diode	904	0.025	0.9	0.9	3.85
HeNe	633	0.43	10.7	0.79	0.22
Nd: YAG/KTP	532	0.2	2.5	0.9	0.45
Argon Ion	488	1.0	3.0	0.9	0.3
XeCl	308	2.5	3.5	0.9	0.2
ArF	193	600	-	0.9	0.02

3.3.3 Solution control

As the procedure of laser generation of acoustic waves, or say, the thermal-elastic analysis is a dynamic multi-physic filed coupling analysis. The result at each time scale is dependent on the movement at last time step. Therefore, the solver type in ANSYS is specified as transient analysis.

The time increment in thermal analysis is set as 1 *ns*, twentieth of the laser pulse duration 20 *ns*, and the solver calculated 1000 steps in total. The time increment in the subsequent mechanical analysis is set following the New Marks scheme:

$$\Delta t = \frac{1}{20 f_{max}}, \tag{3- 17}$$

where f_{max} is the maximum frequency of the laser generated surface acoustic waves, which is decided by the velocity of surface acoustic waves C_R and radius of laser source as shown in the equation (3-2). The radius of laser in model is assumed to be 0.5 *mm*, and C_R is determined by the mechanical properties of material as the shown in the following expression [80, 81],

$$c_R = \frac{0.87+1.12\upsilon}{1+\upsilon}\sqrt{\frac{E}{2\rho(1+\upsilon)}}, \quad (3\text{-}18)$$

where υ is the possion's ratio, ρ is the density and E is the Young's modulus of material. These mechanical properties of material are showed in the Table 3- 3. By calculation, the time increment in mechanical analysis was set as 2 μm and the solver was calculated for 1000 steps in total.

Boundary conditions as described in the section of 3.3.1 were applied on the model. The pulsed laser source was perpendicular incident on the model surface as the heating source and the centre of laser pulse is located at x=0. Table 3- 3 is a summary of the parameters used to define the boundary conditions, in which the laser source is assumed to be Nd: YAG with a wavelength of 532 *nm*.

Table 3- 3 Summary of the parameters for the definition of boundary conditions

Parameters to define the boundary conditions	
Laser radius	0.5 mm
Laser pulse rise time (half pulse duration)	10 ns
Laser penetration depth	0.45 mm
Laser absorption coefficient	0.2 mm^{-1}
Laser scattering coefficient	2.5 mm^{-1}
Laser scattering anisotropy coefficient	0.9
Laser energy	2 mJ
Initial temperature (in thermal analysis)	300 K
Reference temperature (in mechanical analysis)	300 K

3.4 Result and discussion

The out of plane displacement (x component) in time was acquired as SAWs signals. SAWs signals were detected at various points at model surface in sequence, starting from point A (2mm away laser source) and ending up at point D (8mm away laser source) with a uniform

distance distribution of 0.5mm to get enough samples as shown in the Figure 3- 4. Thirteen points were scanned in total, including the point B and C at elastic boundaries.

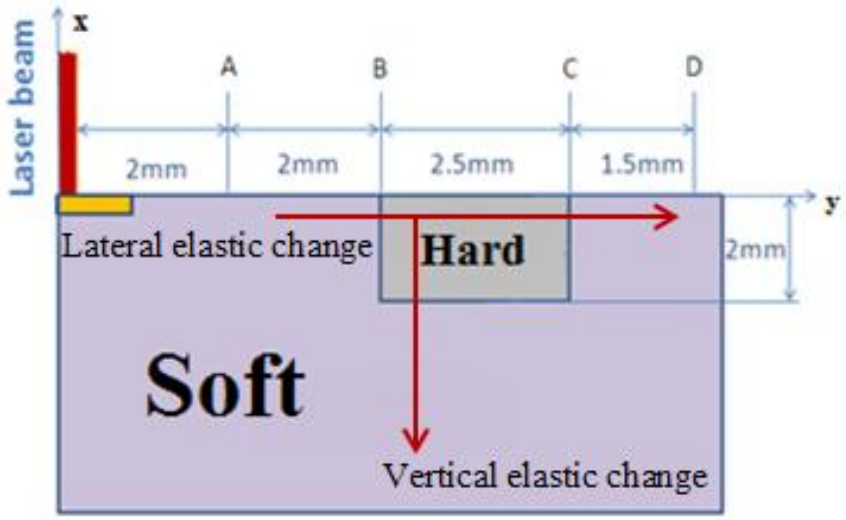

Figure 3- 4 Schematic of signal detection and location.

Figure 3- 5 shows the typical waveform of the simulated SAWs as a function of time. The whole wave signal takes for around 1 *ms* and the waveform consisted of two acoustic pulses. The first peak represented the arrival of longitudinal waves. It came earlier since longitudinal wave propagates at a higher rate than shear wave and surface wave in solid. The second peak was the arrival of real SAWs, which propagated at a lower rate and occupied the majority of acoustic energy. The difference of two wave speed can be also seen from the Figure 3- 6.

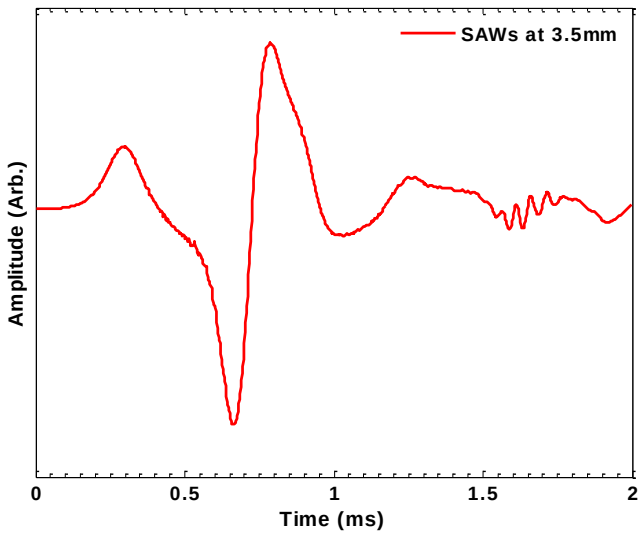

Figure 3- 5 Typical waveform of laser generated SAWs.

Figure 3- 6 shows three SAWs signals detected at three ambient points, at 2.0 *mm*, 2.5*mm* and 3.0 *mm* respectively. It can be seen that time delay between first peaks were much smaller than the time delay between the second major peaks. This also indicated that the first peaks spread at a higher rate and they were actually the longitudinal waves generated by laser heating. The second peaks were the real SAWs. Compared with Figure 3- 5 , the time scale in Figure 3- 6 was also extended, from which something interesting but hidden behind was discovered.

If we look at the signals at 1*ms* and 1.5*ms*, another two wave peaks came out. We call these the third peak and the forth peak. The third and fourth peaks were not expected in typical SAWs waveforms as shown in the published results [82-84]. The reason for this irregularity is the presence of lateral elasticity boundaries at B and C which leaded to SAWs reflection at boundaries and thus generated SAWs echoes. This can also well explain why the 3rd and 4th peaks detected at 3.0*mm* unexpectedly came earlier than the two peaks detected at 2.0*mm*. This is because 3.0 *mm* is closer to the boundaries, thus echoes experienced a shorter path and so it came earlier than the others.

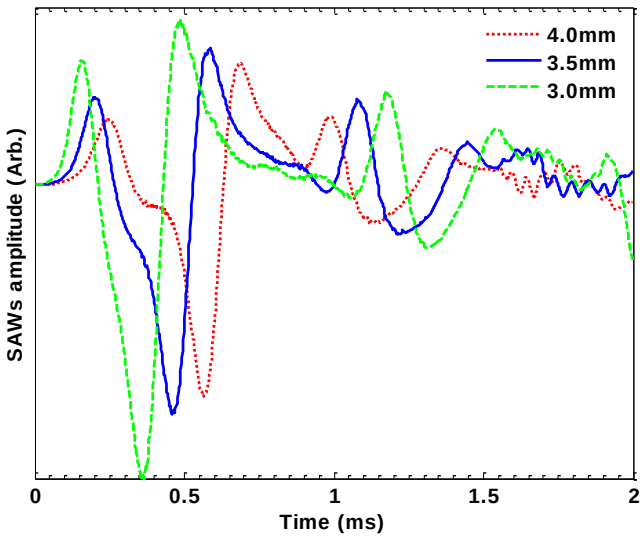

Figure 3- 6 SAWs signals and the echoes reflected from elastic boundary

Figure 3- 7 shows the typical spectrum of SAWs signal. The spectrum was calculated by the standard FFT operator. As shown in the figure, the bandwidth of SAWs signal was

approximately 9kHz, which indicated that SAWs generated by laser pulse are fairly broadband.

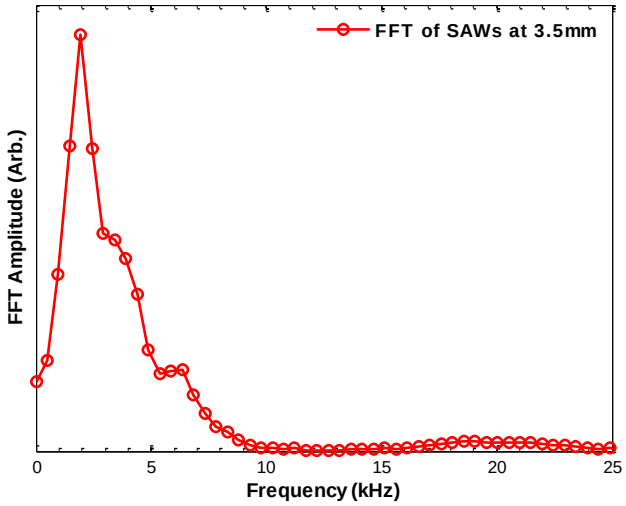

Figure 3- 7 Typical spectrum of simulated SAWs.

3.4.1 Sensing lateral elasticity change by SAWs

As shown in Figure 3- 8, SAWs were detected at various points in sequence, from 2.0*mm* to 8.0*mm* with a distance interval of 0.5*mm*, and propagated through different stiffness regions along the model surface. In this section, SAWs will be used to characterise this lateral stiffness change.

The amplitude of SAWs was traced as the black solid line which is marked with triangles Figure 3- 8. From the amplitude trend we can see SAWs attenuation experienced singularities at elastic boundaries: a sudden dramatic attenuation at the soft to hard boundary and a negative attenuation at the hard to soft boundary. In order to see this more clearly, peak-to-peak amplitudes of SAWs were calculated at each position and Figure 3- 9 shows the normalised results respect to the highest value detected at position A.

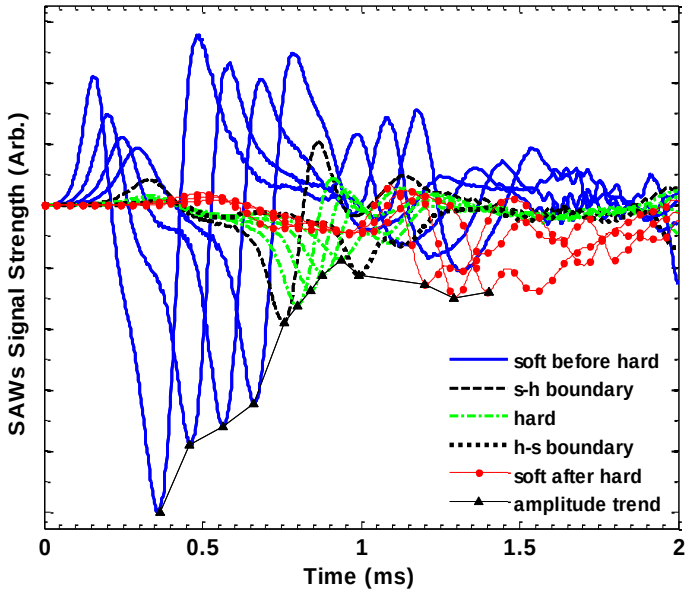

Figure 3- 8 SAWs (out of plane displacement) detected in sequence on model

From Figure 3- 9 we can see, at first, in soft tissue, SAWs peak-peak amplitude attenuated gradually during wave propagation, however, at the elastic boundary of soft to hard (4mm away laser source), the peak-peak amplitude attenuation suddenly become dramatic, from ~0.7 to ~0.38, attenuated approximately 0.32. This is due to hard tissue has larger damped spring-mass system than that of soft tissue, and as a result hard tissue allows smaller acoustic oscillation and thus smaller peak-peak SAWs amplitude, leading to the dramatic SAWs amplitude attenuation at the soft to hard boundary compared with that in pure soft tissue. This indicated that SAWs are sensitive to the elasticity change in the media and the amplitude changes instantaneously at the elasticity boundary.

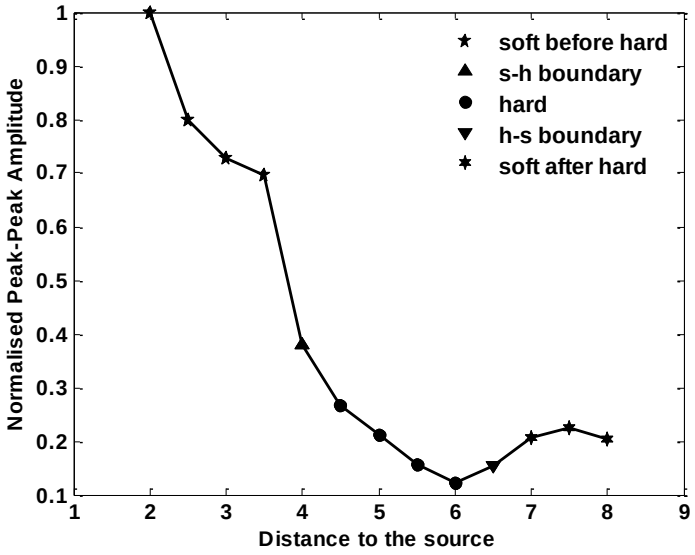

Figure 3- 9 Peak to peak amplitude of SAWs

as shown in Figure 3- 9 SAWs peak-peak amplitude firstly attenuated gradually during wave propagation in soft tissue, at the elastic boundary of soft to hard (4mm away laser source), the peak-peak amplitude attenuation suddenly become dramatic, from ~0.7 to ~0.38, attenuated approximately 0.32. This is due to hard tissue has larger damped spring-mass system than that of soft tissue, and as a result hard tissue allows smaller acoustic oscillation and thus smaller peak-peak SAWs amplitude, leading to the dramatic SAWs amplitude attenuation at the soft to hard boundary compared with that in pure soft tissue. This indicated that SAWs are sensitive to the elasticity change in the media and the amplitude changes instantaneously at the elasticity boundary.

From 4mm to 6.5 mm away laser source, SAWs propagation along the hard tissue surface. When SAWs entered into hard tissue, attenuation of peak-peak amplitude went back to the normal trends again, the amplitude attenuated gradually with wave propagation. However, at the hard to soft boundary (6.5mm), singularity happened once again: the SAWs amplitudes started to increase instead of attenuating- negative attenuation observed and it lasted for a certain distance until SAWs had passed 1mm away the hard to soft boundary at the location of 7.5 mm. This is due to soft tissue allows larger acoustic oscillation hence larger peak-peak amplitude as a result of lower damped spring-mass system compared with that of hard tissue. When this amplitude enhancement (happened as SAWs reached at soft from hard) can overcome the amplitude attenuation due to normal acoustic damping (as long as the stiffness difference beside boundary to be large enough), the overall SAWs amplitude attenuation becomes negative. This was another evidence to support SAWs propagation was sensitive to

the elasticity variation: at hard to soft boundary, SAWs amplitude would suddenly increase, and this situation would last for a distance (from 6mm to 7.5 mm away laser source) to allow the wave development when SAWs are spreading in soft until the amplitude enhancement approaches saturation (at 7.5mm) and since then the wave attenuation would go back to normal state, to be positive again (at 8mm). Therefore, SAWs amplitude trend was proved to be a good reference to locate the elasticity variation on the model surface.

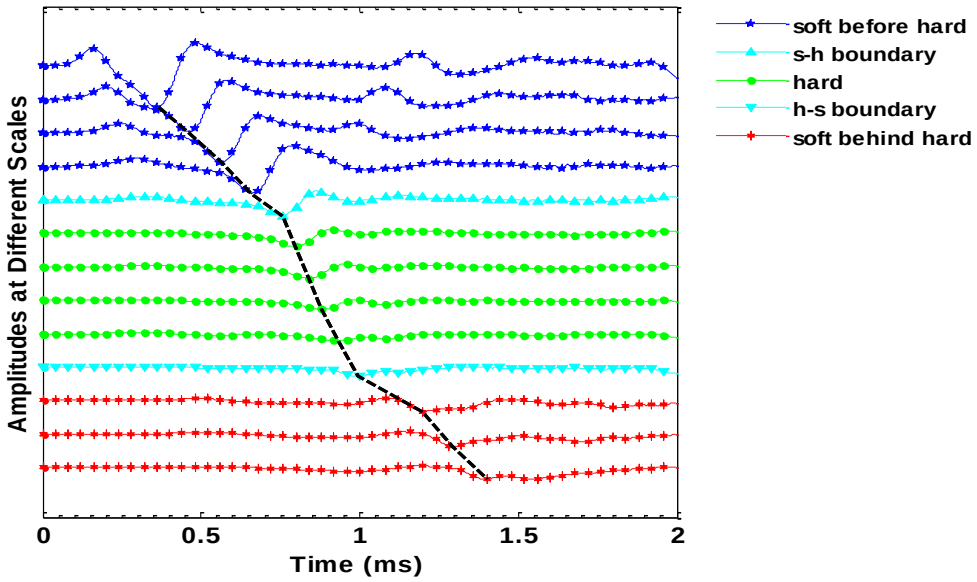

Figure 3- 10 SAWs signals plotted at different scales. The dashed line connected all the wave troughs, from which the time delay at each detection points can be seen.

The Figure 3- 10 shows the SAWs in different scales, from which the time delay between each can be clearly seen after connecting all the wave troughs. As shown from figure, time delay between adjacent SAWs kept nearly the same except the sharp changes existed at the elasticity boundaries. It can be also seen that the time delay in soft tissue was obviously larger than those in the hard tissue. As the distance between adjacent SAWs were known as 0.5 mm, and then the group velocity at different locations can be calculated, which was shown in the Figure 3- 11.

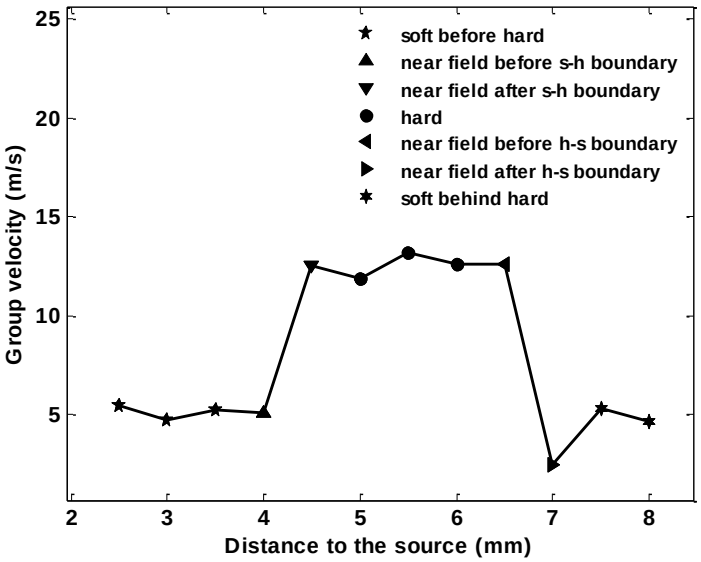

Figure 3- 11 SAWs group velocity trend

Before the hard region, 2mm to 4mm away laser source in the soft tissue, the group velocity of SAWs approximately estimated as 5 m/s. This value suddenly increased to 12.5m/s at the boundary of soft-to-hard and stayed at the same level with slight fluctuation until SAWs reached another boundary, hard-to-soft, at the other end. At this point, the group velocity came down to ~5 m/s again and stayed at the same level when SAWs passed away the hard region into the soft tissue. Therefore, group velocity of SAWs was sensitive to the elasticity variation: faster in hard medium while slower in soft medium, in addition, by calculation of SAWs group velocity, the elasticity in each part can be estimated from the equation (3-18).

Table 3- 4 Comparison between Young's modulus measured from SAWs group velocity and the values originally specified in model

Young's modulus (Pa)	By estimated	Input	Deviation	Deviation ratio
Soft tissue	87648	87097	551	0.63%
Hard tissue	558140	511147	46993	9.1%

Table 3- 4 is a comparison between the Young's modulus in soft and hard that were estimated from the simulated group velocity and that were originally specified in the modelling model. The deviations between can come from the finite element computation error and the potential error from equation (3-18). Nevertheless, the error ratios are within plus-minus 10%, an

acceptable deviation range, therefore the group velocity of SAWs can be used to quantify the elasticity change distributed in lateral along the model surface.

As stated above, the elasticity change along model surface can be unveiled either from the observation of SAWs amplitude trend or the estimation of group velocity variation. However, SAWs analysis in time domain only provided the information of lateral elasticity variation. For sensing vertical elasticity variation, the spectral analysis of wave speed, SAWs phase velocity, is necessary.

3.4.2 Calculation of phase velocity

Phase velocity is defined as the speed at which the phase of any one frequency component of a wave propagates. Phase velocity of SAWs can be regarded as a spectral analysis of the surface wave speed. In homogeneous materials, phase velocity of SAWs is expected to be identical at each frequency. However, dispersion would be observed when it comes to a multi-layer medium, in which each layer has different elasticity. The phase velocity of SAWs is influenced by the mechanical properties of all layers it penetrates to. High frequencies with a shorter wavelength penetrate shallow depth and the velocity is dependent on the superficial layer. Low frequencies with a longer wavelength penetrate deeper, and the velocity is determined by the subtractive layer.

The phase velocity of SAWs can be calculated by the measurement of phase change with respect to the wave path length as follows [13]:

$$C_R = 2\pi f|\Delta r/\Delta\varphi|, \tag{3- 19}$$

where C_R is the SAWs phase velocity at a frequency of f, $\Delta\varphi$ is the phase change respect to a wave path length of Δr.

The phase change $\Delta\varphi$ can be solved from the cross-correlation spectrum of signals as shown below [13]:

$$\Delta\varphi = \arctan\frac{\mathrm{Im}(U_1(\omega)\overline{U_2(\omega)})}{\mathrm{Re}(U_1(\omega)\overline{U_2(\omega)})}, \tag{3- 20}$$

where U_1 and U_2 are the Fourier transform of signals detected at the two points on sample surface, $\overline{U_2(\omega)}$ denotes for the conjugate function of U_2. The MATLAB codes for signal processing are attached in the Appendix A.

3.4.3 Sensing vertical elasticity change by SAWs

Four points have been chosen to calculate the SAWs phase velocity; two were picked at soft tissue surface, 2mm and 3mm away laser source, between which the tissue is homogenous in both lateral and vertical direction. The other two were picked on the hard tissue surface, 5mm and 6 mm away laser source, where the tissue is localised homogenous in lateral but heterogeneous at depth. The phase velocity at two sites was calculated and shown in the Figure 3- 12 . The dashed lines are linear fitting of the phase velocity data.

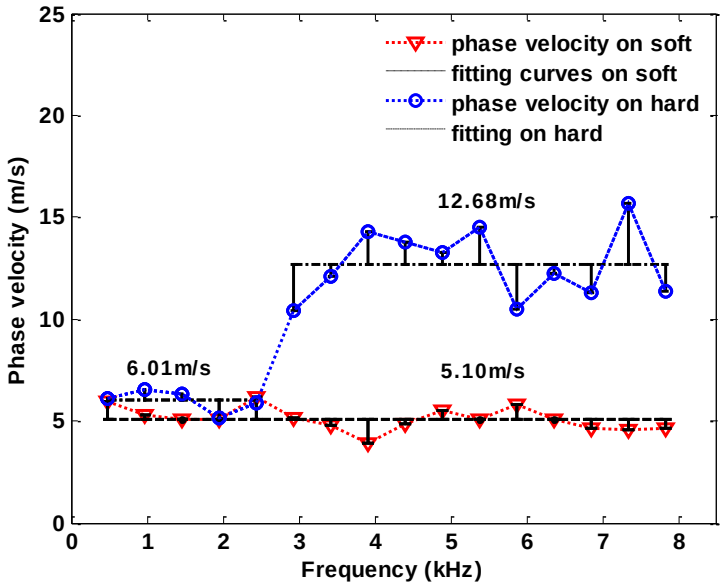

Figure 3- 12 SAWs phase velocity on soft tissue and hard tissue

In the homogenous soft region (red line marked with triangle), phase velocity has no distinct dispersion and it was averagely estimated as 5.10 m/s, close to the group velocity value 5 m/s in the soft tissue. However, at the hard tissue surface (blue lines marked with circle), the phase velocity became significantly dispersed above 2.5 kHz and the high frequency content approximately falls in the level of 12.68 m/s which was closed to the group velocity value 12.5 m/s in hard tissue. The averaged value of low frequency content on hard (6.01 m/s) coincided with that on the soft (5.10 m/s), and it actually reflected the wave speed in the soft tissue which was located below the hard surface layer. Therefore, from the analysis of phase velocity dispersion, the elasticity change hidden in depth can be successfully identified.

Note that, the frequency at which phase velocity start to disperse should be the frequency at which SAWs penetrates to the elastic boundary (hard to soft) at depth. Thus the wavelength of this frequency content can be calculated by the wave velocity in soft (6.01 m/s) times the

reciprocal of dispersion frequency (1/2.5 kHz^{-1}), which equals 2.4 mm. The value corresponded with the surface layer (hard tissue) thickness, 2.0 mm, with an error ratio of 20% in this case. Therefore the dispersion frequency can be a potential reference to estimate the thickness of sample surface layer.

3.5 Conclusion

In this chapter, SAWs were generated thermal-elastically by a laser pulse and the SAWs propagation on a heterogeneous tissue model was investigated by the FEM. A relative stiff region was embedded on the surface of tissue model to stimulate the sclerosis. The result shows that wave attenuation and group velocity of SAWs were sensitive to the lateral elasticity change in tissue, while the phase velocity dispersion can be utilised to sense the vertical elasticity variation. The results and supposes obtained by the modelling study were validated and strengthened by experiments in the next chapter.

Chapter 4 Experimental study of using SAWs to characterise tissue

Introduction

In the last chapter, SAWs showed the ability to sense both lateral and vertical elasticity variation from a simulation study. In this chapter, results and supposes from the modelling will be validated and strengthened by experiments. In the experiment, SAWs were excited by an electro-magnetic shaker (mechanically) instead of using a laser pulse (thermal-elastically) due to availability in the lab during the study. Even though SAWs are generated with different mechanism in simulation and experiment, validation of simulation results by the experiment still holds because our measurement interest is the velocity of SAWs, which is essentially determined by the mechanical properties of sample rather than the generation mechanisms.

This chapter is organised as follows: experimental platform was introduced at beginning, including the wave generation method, wave detection system, scanning scheme and the tissue-mimicking (TMM) phantom fabrication process. Then experiment firstly conducted on a set of single-layer homogeneous TMM phantoms made with different agar concentrations to vary the stiffness. Young's modulus of each was estimated from the SAWs phase velocity and then compared with those measured from an independent mechanical compression test to validate SAWs measurement. After this, a heterogeneous two-layer phantom was made with a known surface-layer thickness to investigate the mechanical characterisation of layered structure and the thickness measurement using SAWs phase velocity dispersion. At last, an *ex-vivo* pig liver was tested to validate the proposed method in real biological tissue environment. The elasticity and thickness measurement by SAWs were finally compared with the published elasticity results and thickness imaging by high frequency ultrasound imaging (HFUI) to evaluate the measurement accuracy.

4.1 Experiment platform

A schematic of the experiment platform was shown in the Figure 4- 1. SAWs were generated by an electro-magnetic shaker which is driven by a function generator, and detected by a laser vibrometer that is synchronised with SAWs generation by the function generator. The shaker moved by a robotic arm to scan the sample and detect SAWs at difference locations, and a PC was used to communicate with robotic arm. Samples include TMM phantoms and an *ex-vivo* pig liver.

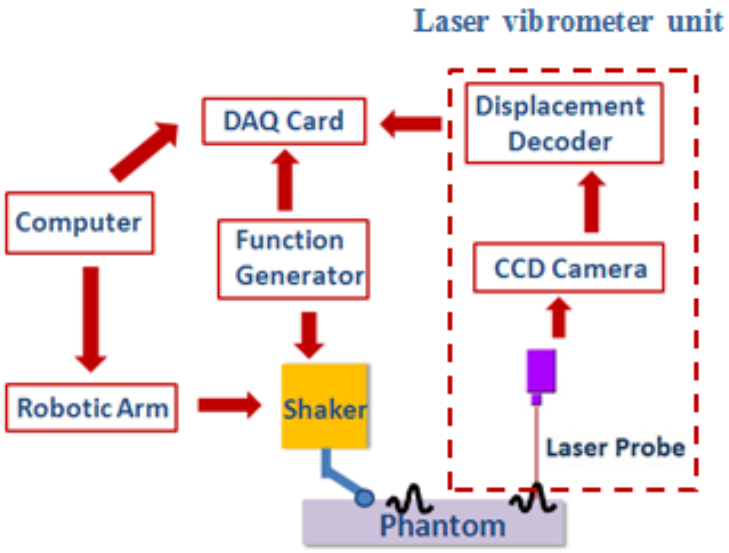

Figure 4- 1 Schematic of experiment platform

4.1.1 Tissue mimicking phantom fabrication

At initial, agar phantoms were used in the experiments to mimicking acoustic and mechanical property of human tissue. Both homogenous and heterogeneous (two layer with different stiffness) phantoms were made to validate the method from simple to complicate. Homogenous phantoms were made as two groups. In the 1st group, phantoms were made of 1.0%, 2.0% and 3.0% agar concentration in weight, with relatively large difference in concentration thus large difference in stiffness. In the 2nd group, phantoms were made with 0.8%, 1.0%, and 1.2% agar concentration in weight, with a relatively small difference in concentration and stiffness. The reason for making such two group phantoms is to study the sensitivity of SAWs stiffness measurement. Also, phantoms in the 2nd group were generally softer than the ones in 1st group, allowing the investigation of stiffness effect on the SAWs measurement bias. All phantoms were made in round with a radius of 60 *mm* and thickness of 25 *mm,* and the surface were flat and smooth, also painted with Indian ink to enhance the optical reflection to increase the signal to noise ratio of laser vibrometer. Heterogeneous phantom was made as two layers. The surface layer was made of 1.2% agar in a known thickness of 5 *mm,* and the subtractive layer was made with 0.8% agar concentration in a thickness around 20 *mm*. Procedures of making TMM phantoms are described as below:

1. Take 110ml distilled water and heat it above 90 °C. (Considering evaporation, the distilled water should be more than ideal value 100ml).

2. Stir the boiled water and pour into already weighted agar (e.g. 1g for 1% agar phantom, 2g for 2% agar phantom and 3g for 3% agar phantom).
3. Keep stirring and heating the water until all agar resolves when liquid looks transparent without any impurity.
4. Stop heating when liquid remain exactly 100 ml. Wait for the liquid cooling down to 40 ~ 50 °C.
5. Pour dark inks and stir with a relative low speed (avoid bubbles). Keep stirring for around 5 minutes.
6. Wait for the liquid cooling to 30 ~ 40 °C, then pour into container for modeling.
7. Repeat the above steps and pour the agar liquid onto an already solidified agar phantom (with different agar weight concentration) to fabricate the two-layer heterogeneous phantom.

Figure 4-2 is a picture showing the phantoms made in such way.

Figure 4- 2 Fabricated TMM agar phantoms made with 1% (1), 2% (2), 3% (3) agar concentration in weight

4.1.2 SAWs generation

An electromagnetic shaker is used to generate SAWs by delivering transient mechanical impulses on the sample surface. Theory of mechanical generation of SAWs was introduced in the section 2.4.1. A line-source design was attached to the shaker head, as shown in Figure 4-3) to generate SAWs in a stronger signal strength compared with using a ball-shape source. The driving signal is set as square stimulus at 50Hz with a duty cycle of 50%. Peak-peak voltage amplitude is set to 5V and has an offset of 2.5V.

Figure 4- 3 Line-source design: a bar attached to shaker head to enhance the SAWs signal strength to get good SNR

4.1.3 SAWs detection

SAWs are detected by Laser-vibrometer unit (Polytec, OFV-534) based on the principle of interference and Doppler frequency shift (page 21). The vibrometer head (Figure 4- 4) includes a laser unit and a sensor head. The laser unit contains a Helium-Neon laser delivering its 633 nm laser light via an optical fibre to a high precision interferometer in the vibrometer head. The laser light splits into a measurement beam and a reference beam. The measurement beam is incident on the test object. The back scattered light is shifted slightly in frequency by the Doppler Effect and contains the displacement and velocity information of test object. A photo detector converts the optical signal created from the interference of the reference beam with the back scattered light into a frequency modulated electrical signal. This signal is then sent to a decoder circuit in the vibrometer controller where the frequency modulated signal is converted into a voltage signal proportional to either velocity or displacement.

Figure 4- 4 Laser vibrometer head (Polytec, OFV-534)

Laser was perpendicular incident on the sample to detect the out of plane displacement of surface vibration as SAWs signal. The distance between vibrometer head and sample are fixed at stand-off distance, 295*mm*, to ensure the visibility maxima of optical detector.

4.1.4 Scanning scheme

As shown in the equation (3-19), in order to calculate the phase velocity dispersion SAWs need to be detected at various distances away the wave source to get the wave path length Δr . This can be achieved either by scanning the detection probe (laser vibrometer head) and fixing the generation applicator (electromagnetic shaker) or by scanning the generation applicator and fixing the detection probe. In our system, we chose the latter scheme because the optical signals scattered/reflected back from the TMM phantoms/pig liver were very sensitive to the sample surface condition, and only at a few detection points on the sample surface the SNR of laser vibromter system can reach the maximum. Therefore the laser vibrometer head was fixed on a tripod once it had been adjusted to reach the maximum SNR level, and the SAWs generation applicator- electromagnetic shaker (wave source) was scanning to get the wave path length Δr for calculating the phase velocity of SAWs.

As the calculation of SAWs phase velocity is not only related to the wave path length Δr but also the phase change $\Delta\varphi$ during wave spreading (equation 3-19). Therefore the wavefront of SAWs need to be precisely matched at each detection points to ensure the phase velocity calculation accuracy. To do so, in our system, the centre of shaker bar was aligned with the laser detection probe and the wave source (electromagnetic shaker) was moving on a robotic arm to ensure all the detection points to be aligned along the SAWs wavefront propagation path (Figure 4- 5).

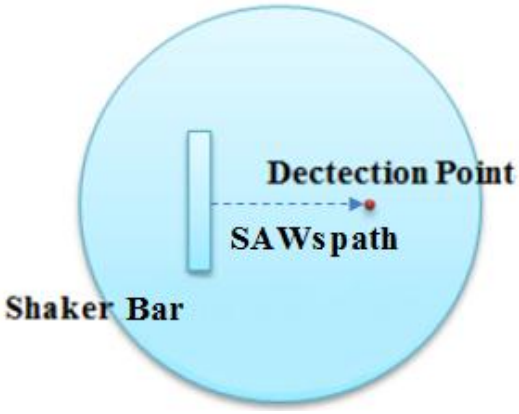

Figure 4- 5 Schematic of shaker alignment with detection points.

The shaker was attached to the robotic arm in a special designed holder as shown in Figure 4-6, in which the shaker was fixed by four bolts. Robotic arm communicated with PC via RS-232 port and the interface is programed in Labview. The front and back panel were attached in appendix C.

In each test, shaker scanned 5 points along the SAWs wavefront propagation path with an interval step of 1mm from far to near the laser detection probe.

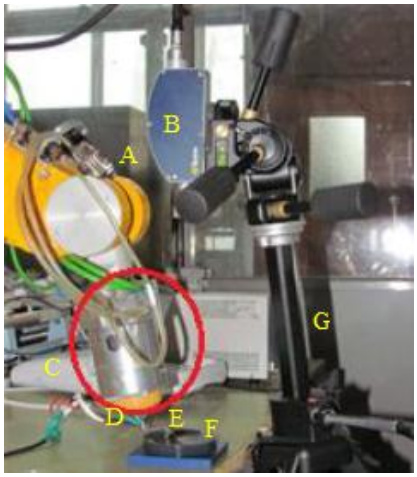

Figure 4- 6 Scanning system: Robotic arm (A), Laser vibrometer head (B), Electromagnetic shaker holder (C), Electromagnetic shaker (D), Shaker bar (E), TMM phantom (F), Tripod (G)

4.2 Results in Homogeneous TMM phantoms

4.2.1 SAWs signal in time and spectrum

Typical waveform of SAWs on homogeneous agar TMM phantoms can be seen from the Figure 4- 7. Similar with the simulated results in Figure 3- 5 SAWs presented in a pulse shape, where low frequencies sustained several milliseconds as the body wave and some high frequencies were concomitant at the start and the end of the pulse. A difference between the simulation and experiment is that longitudinal wave (the 1st peak) in Figure 3-5 was very small here. This might be due to the viscocity dampping in phantom, leading to a sigfinicant attunation of longitudianl waves. The viscocity character of tissue was not considered in the simulation.

Figure 4- 8 shows the typical spectrum of SAWs signal, in which amplitude was normalised respect to the maximum value. Due to viscosity damping in TMM phantoms, the strength of spectrum 2, detected at 9*mm*, was lower than the strength of spectrum 1 that was detected at

7*mm* away the wave source. In a distance of 2*mm*, signal strength attenuated 45%, which indicated that the viscosity damping had a significant effect on SAWs propagation. Therefore, in the future work, simulation work needs to be refined by accounting tissue viscosity in the model.

Cross-correlation spectrum of two signals was also shown in the Figure 4- 8, based on which phase velocity of SAWs was calculated later. To ensure SAWs signal are dominated by useful signals rather than random noises, a frequency cut-off was made at where SAWs signal dropped off 40dB respect to the peak. The frequency cut-off was finally determined as 4 *kHz* in this case, and in the following analysis, only phase velocity below this cut-off were presented to ensure the measurement accuracy.

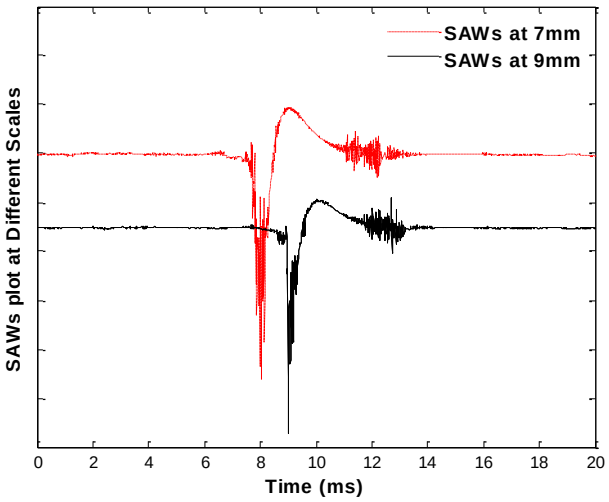

Figure 4- 7 Typical SAWs waveforms that were detected on 1% agar TMM phantom

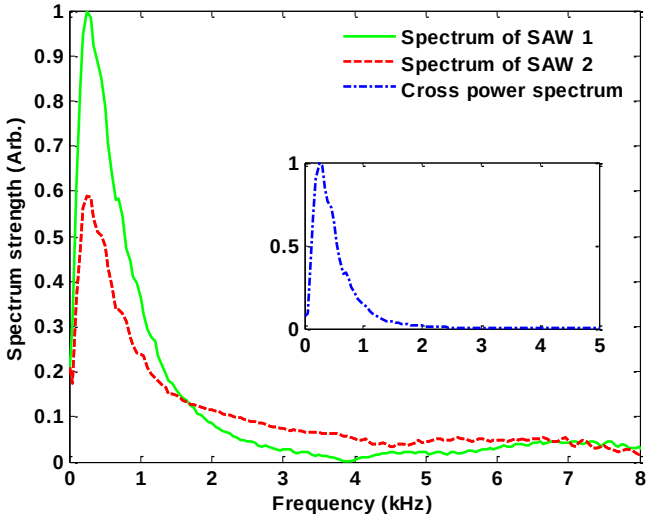

Figure 4- 8 Typical spectrum of SAWs on 1% agar phantom and their cross-correlation spectrum.

4.2.2 Phase velocity of SAWs on soft TMM phantoms

SAWs phase velocity on 0.8%, 1.0% and 1.2% agar phantoms were shown in the Figure 4- 9. Generally, in each phantom, phase velocity has no distinct dispersion as expected, since the phantoms were homogeneous and the elasticity was distributed uniformly at different depth. The slight fluctuations (no more than 0.2m/s) in the figure may be due to the system measurement error, therefore, linear fitting was used to trace the trend of phase velocity curves. As we can see from the figure, the stiffer the phantom is, the faster the SAWs phase velocity is. This corresponded to the consequence of equation (4-3). The values of phase velocity were estimated by averaging the wave speeds at each frequency, and they were 1.96 m/s, 2.33 m/s and 2.72 m/s, respectively, on 0.8%, 1.0% and 1.2% agar phantoms.

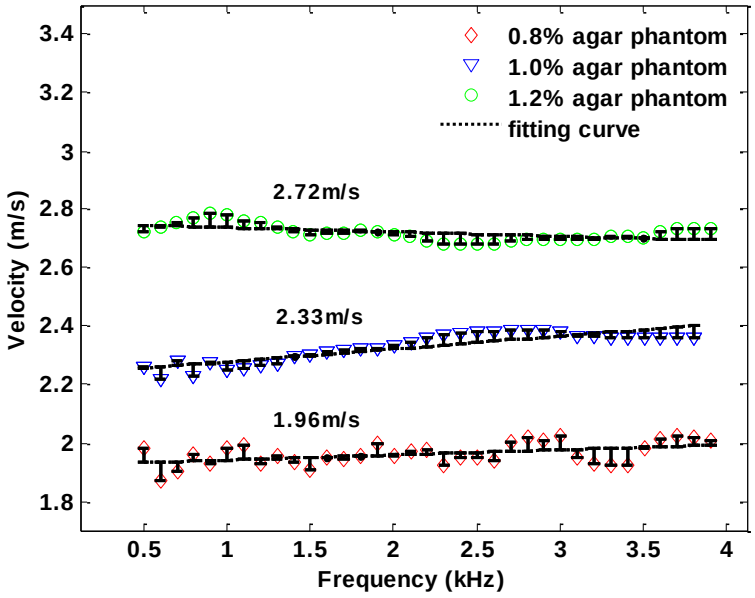

Figure 4- 9 SAWs phase velocity on homogeneous agar phantoms

4.2.3 Simplified relationship between SAWs velocity and elasticity

As introduced in page 13, SAWs field can be solved from the well-known Rayleigh equation,

$$R(\xi) = ((\gamma^2 - 2\xi^2)^2 - 4\xi^2\sqrt{\xi^2 - \gamma^2}\sqrt{\xi^2 - 1}), \quad (4\text{- }1)$$

Exact solutions of the Rayleigh equation have been extensively studied in [68-70], the ratio of shear wave and surface wave velocity was derived and given by,

$$\frac{C_T}{C_R} = \sqrt{\frac{0.58+\nu/(1-\nu)}{0.44+\nu/(1-\nu)}}, \quad (4\text{- }2)$$

where ν is Poisson's ratio of material.

Since Poisson's ratio of biological soft tissues are quite similar, within a narrow range between 0.49 to 0.499, equation (4-2) has been further simplified to $C_T/C_R = 1.05$ in soft tissues, and the SAWs speed can be related to the Young's modulus by [9],

$$c_R = \frac{1}{1.05}\sqrt{\frac{E}{3\rho}}\ , \tag{4- 3}$$

which is actually a simplification of equation (3-18). Therefore the Young's modulus can be estimated from SAWs speed as long as the density of material is known. Densities of three phantoms were 1.008 kg/m^3, 1.010 kg/m^3, and 1.020 kg/m^3 for 0.8%, 1.0%, and 1.2% agar phantom. By equation (4-3), Young's modulus of three phantoms were then inversed out, which were 12.51 *kPa*, 16.35 *kPa*, and 21.72 *kPa* respectively, showing a good stiffness gradient as expected.

4.2.4 Verification of elasticity measurement

In order to verify the elasticity measurement by SAWs, an independent compression test was conducted to provide a reference of the real phantom elasticity. The compression testing platform (Tinius Olsen H5KS) was shown in the Figure 4- 10.

TMM phantoms were placed on the stage and compressed by a force applicator until it became fracture. Stress-strain relationship was recorded by the stress and strain sensor, and by using the linearly fitted part (Figure 4- 11), Young's modulus of each phantom was calculated by the following equation:

$$E = \frac{l}{s}\cdot\frac{\partial F}{\partial \varepsilon}\ , \tag{4- 4}$$

in which F is the compression stress measured by force sensor, ε is the phantom strain in compression direction, l is the height of phantom, and s is the contact area between phantom surface and the compression applicator.

Young's modulus of three phantoms measured from compression test were shown in the Table 4- 1, and Figure 4- 12 gave a comparison of the results measured from SAWs method and the compression test.

Table 4- 1 Young's modulus (E) measured from SAWs phase velocity and the independent compression test

Phantoms	SAWs phase velocity	Young's modulus (SAWs method)	Young's modulus (compression test)	Deviation
0.8% agar	1.96	12.51	13.51	7.35
1.0% agar	2.33	16.35	18.70	12.56
1.2% agar	2.72	21.72	24.74	12.20
Units	*(m/s)*	*(kPa)*	*(kPa)*	*%*

Figure 4- 10 Compression test platform (Tinius Olsen H5KS)

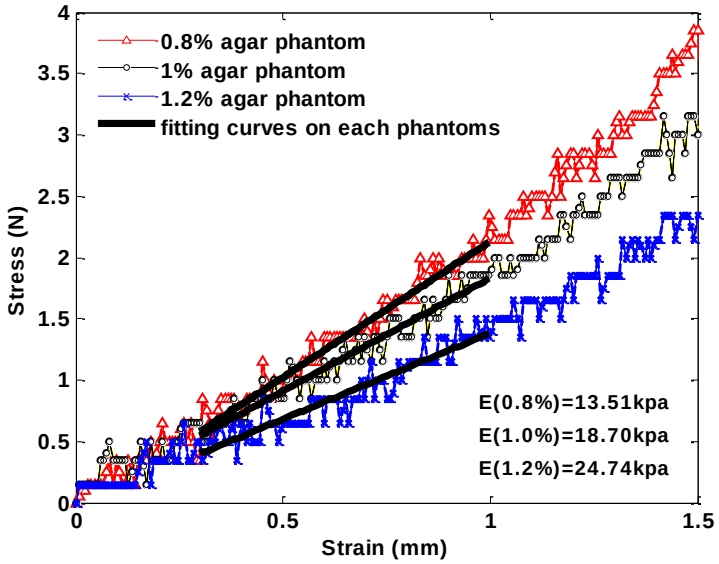

Figure 4- 11 Stress-strain plot from the compression test to measure the phantoms elasticity

In general, elasticity measurement by SAWs was slightly lower than that of compression tests. Deviations between were 0.99 *kPa* for 0.8% agar phantom, 2.35 *kPa* for 1.0% agar phantom, and 3.02 *kPa* for 1.2% agar phantom, and all error ratios fell within the range of 13%. This indicated that elasticity measurement by SAWs phase velocity has good performance and it can be used to characterise the mechanical property of homogeneous TMM phantom with acceptable measurement error.

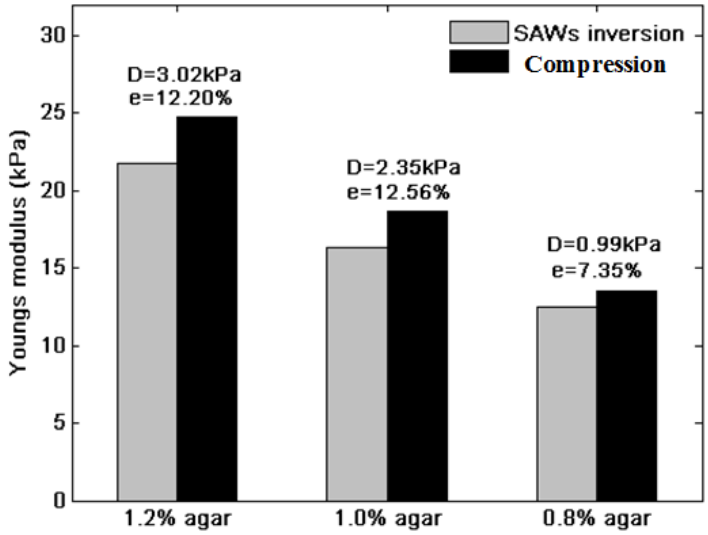

Figure 4- 12 Comparison of Young's modulus measured from SAWs phase velocity and independent compression test

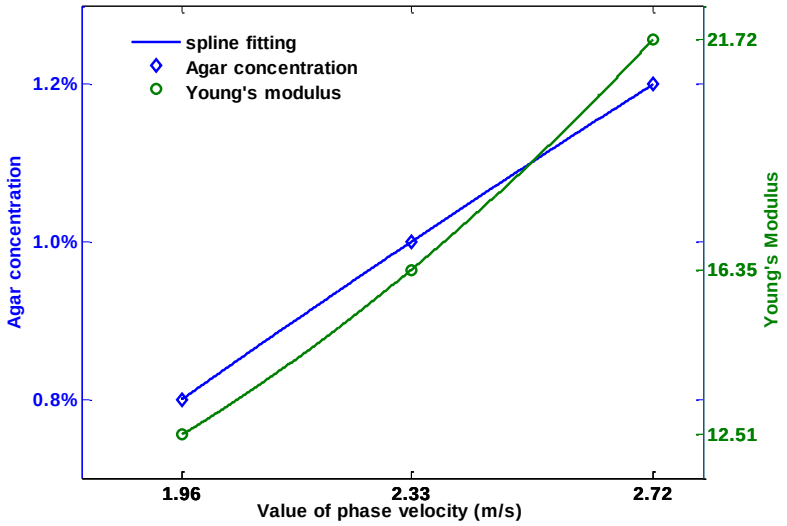

Figure 4- 13 Relation between phase velocity and the concentration and stiffness of phantom.

Figure 4- 13 showed the relation between phase velocity and phantom stiffness and concentration. Spline interpolation was used to predict the regression relationship. As we can see from figure, the phase velocity increased linearly with agar concentration, while it increased exponentially with phantom stiffness, which corresponded with the consequence from equation (4-3).

4.2.5 Measurement bias in soft and hard TMM phantom

SAWs phase velocity of the 2nd group TMM phantoms (stiffer) was also tested to investigate the stiffness effect on measurement accuracy. Tests were performed 1%, 2% and 3% agar phantoms. The SAWs phase velocity of each was plotted in Figure 4- 14, in which error bars indicated the standard deviations among five repeated tests.

As seen from the figure, fluctuations of phase velocity in harder phantoms were generally larger than those of softer phantoms (e.g. between 0.5-1.5 kHz in 2% and 3% agar phantoms), and phase velocity of SAWs on 1% homogenous agar phantom had the least fluctuations. From the deviations between mean values and extrema (error bar), it can be also concluded that SAWs phase velocity measurement has smaller bias in soft sample, in terms of both higher measurement accuracy and higher measurement stability. However, we should note that the phase velocity of 1% agar phantom in figure 4-14 is slightly smaller than that in figure 4-9. The deviation of phase velocity could result from the difference in agar concentrations of two individual 1% agar phantoms that were fabricated separately in each test. To fabricate a 1% agar phantom, 1g agar powder was weighted and dissolved in 100 ml water. Because the accuracy of our scale is 0.1g, the difference in agar concentration can be as high as 20% (e.g. in the extreme situation: 0.9 g agar is weighted to fabricate the 1st phantom and 1.1 g agar is weighted to fabricate the 2nd phantom, then the difference in agar concentration is 20%). As a result the phase velocity of SAWs measured from two individual 1% agar phantoms can be deviated as high as 20% because the phase velocity is proportional to the agar concentration, given in the figure 4-13.

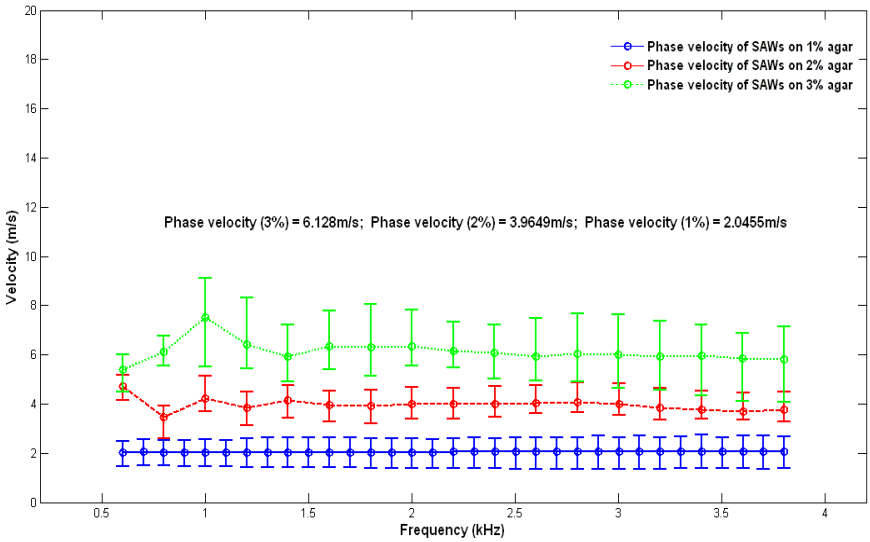

Figure 4- 14 SAWs phase velocity on 1%, 2% and 3% agar phantoms4.3 Results on two-layer heterogeneous TMM phantom

In order to study the feasibility of using SAWs to give a mechanical characterisation of layering-featured structure, heterogeneous two-layer TMM phantoms were fabricated and tested in this section. The heterogeneous phantom consisted of a surface layer made of 0.8% agar and a substantive layer made of 1.0% agar. The phantom was made to be relatively soft to mimicking the real tissue condition. Another reason is that smaller measurement bias is expected from relative soft samples. The thickness of surface layer was 5 mm and the whole phantom was 20 mm in height. The thickness of the surface layer of our phantom is much thicker than the real epidermis layer of tissue; however, the aim of the very initial experiment here is to investigate whether SAWs phase velocity dispersion has the ability to identify different layers in a heterogeneous structure. Therefore the thickness of the surface layer of phantom is made to be relatively large in order to get an easier measurement of the surface layer thickness in the initial experiment exploration. In 4.4, test on ex-vivo porcine liver with a realistic surface layer thickness will be conducted to evaluate the possibility of epidermis thickness evaluation.

4.3.1 Temporal and spectrum of SAWs in two-layer TMM phantom

The typical SAWs waveforms and spectrum in two-layer TMM phantoms were shown in the Figure 4- 15 and Figure 4- 16. Compared with SAWs in homogenous phantoms, the waveforms in the heterogeneous phantom were heavily distorted. Instead of a single wave cycle observed in Figure 4- 7, another minor cycle came out just before the arrival of dominant peak. The

difference can be also seen from the SAWs spectrum. In the heterogeneous phantom, dominant wave energy still located at low frequencies, while different with that in homogenous phantom, another peak occurred in the spectrum around 1 kHz. The dominant peak at hundreds hertz (lower frequency) corresponded to the large wave cycle in time, and the 1 kHz spectrum (higher frequency) corresponded to the minor wave cycle which came earlier in time. Reason for this wave distortion in time and frequency might be due to the elasticity boundary at depth which potentially affected the SAWs penetration.

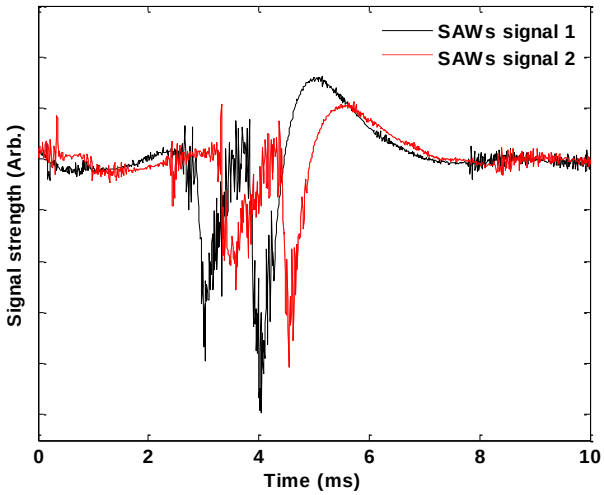

Figure 4- 15 SAWs waveform in heterogeneous agar phantom.

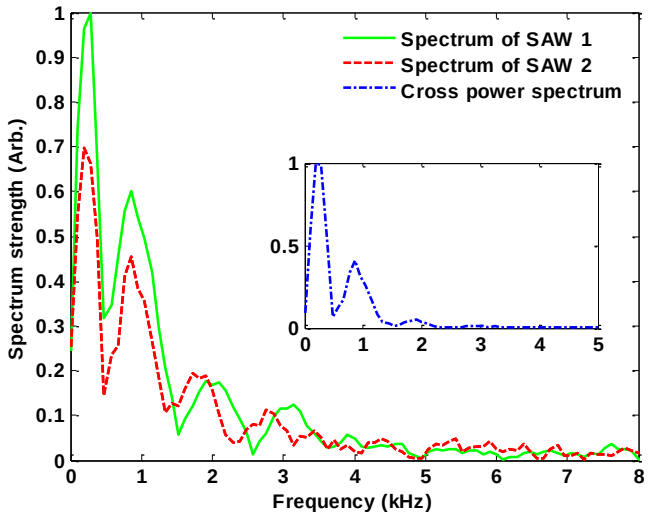

Figure 4- 16 Frequency responses of SAWs in heterogeneous agar phantom

4.3.2 Phase velocity of SAWs in two-layer TMM phantom.

The phase velocity of SAWs in the heterogeneous two-layer phantom was shown in the Figure 4- 17 Compared with homogeneous phantoms (Figure 4- 9), phase velocity in two-layer

phantom dispersed apparently and it was divided into two distinct levels at the frequency around 0.5 kHz due to the different stiffness in surface layer and subtractive layer. Velocity at lower frequency had a mean value of 2.41 m/s, which was determined by the mechanical property of subtractive layer made of 1.0% agar concentration. This value matched well with 2.33 m/s, the phase velocity measured on the homogeneous 1.0% agar phantom. Velocity at high frequency was estimated as 1.86 m/s, close to 1.96 m/s, which was measured on the homogenous 0.8% agar phantoms. Therefore, the phase velocity was indeed sensitive to the elasticity change along different layers, and the high frequency characterised the surface layer while the low frequency characterised the subtractive layer. Based on equation (4-3), Young's modulus of each layer were then inversed as 19.31 *kPa* for subtractive layer and 11.50 *kPa* for surface layer, with error ratios of 3.26% and 14.88% respectively, respect to the Young's modulus measured from the independent compression tests.

In clinical practice, besides stiffness quantification, locating of the elasticity change was also important for diagnosis and treatments. As described previously, surface layer of this heterogeneous phantom was made as 5.0*mm* in height, thus, the elasticity boundary was just located at the same depth 5.0*mm* underneath the surface. In order to predict this from SAWs phase velocity, the attribution of SAWs penetration should be considered. SAWs perpetration is comparable to one wavelength which is the product of SAWs phase velocity and the reciprocal of its corresponding frequency. In Figure 4- 17 , phase velocity became dispersed at 0.5k*Hz*, which means that it was at this frequency, 0.5k*Hz*, SAWs penetration can exactly reach the elasticity boundary at depth. Therefore by dividing 2.41*m/s*, the phase velocity of subtractive layer, by 0.5*kHz*, the frequency at which phase velocity started to be dispersed, the penetration and thus the location of elasticity boundary can be estimated as 4.82*mm* underneath the surface. This value was close to the real location at 5.0*mm*, with an error ratio of 3.6%. Therefore SAWs phase velocity dispersion can be also used to estimate the location of elasticity boundary at depth.

In summary, by studying homogenous and heterogonous phantoms in this section, SAWs showed the ability to give a mechanical characterisation of TMM phantoms, in terms of both stiffness quantification and stiffness boundary locating. In the following, experiments were conducted on an *ex-vivo* pig liver to provide a further validation of our method in real biological tissues.

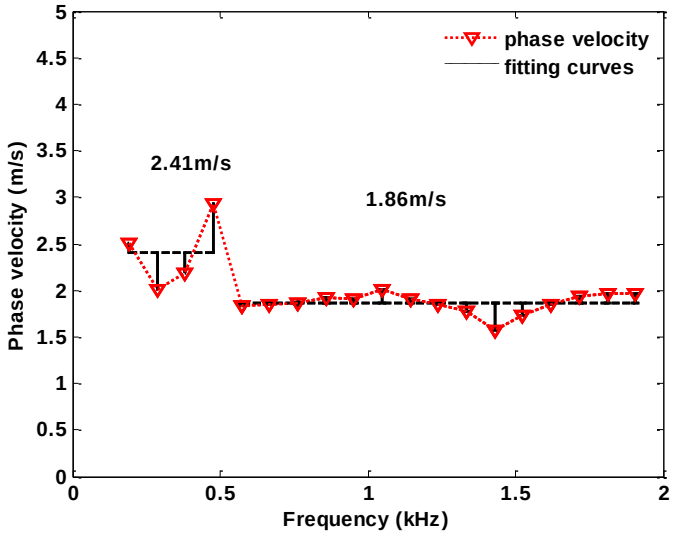

Figure 4- 17 SAWs phase velocity in two-layer heterogeneous agar phantom.

4.4 Results in ex-vivo biological tissue

Figure 4- 18 showed the phase velocity of SAWs evaluated at different locations along wave propagation in a fresh pig liver. Phase velocity dispersions were observed since liver cuticle is stiffer than the inner tissue. Phase velocities were then inverted to Young's modulus to quantify the liver elasticity, and using the same method described in *4.3.2*, the depth of elasticity boundary, thus the thickness of liver cuticle was estimated. These parameters were summarised in Table 4- 2.

As shown in Table 4- 2, Young's modulus of liver inner tissue ranged from 0.86 *kPa* to 1.77 *kPa*, corresponding well with the published result in [42]. Stiffness of liver cuticle were averaged as 2.97 *kPa*, slightly stiffer than the inner tissue as expected, however, there was no reference available to validate this value for cuticle.

The thickness of liver cuticle was estimated at 0.22 ± 0.11 *mm*. The thickness measurement was then validated by the high frequency ultrasound imaging (HIFU). Figure 4- 19 showed the longitudinal section of liver imaged by HIFU. The resonant frequency of ultrasound transducer was 150 MHz, providing a good resolution to identify the thickness of liver cuticle. The relatively dark region, as shown between the dashed lines, represented the liver cuticle, and the bright region below was the liver inner tissue. The area above dash line (brightest in image) was water, which was used for the acoustic impedance matching with ultrasound imaging transducer. By calculating the distance between two dash lines, the thickness of cuticle was estimated as 0.23 *mm*, agreed with the SAWs measurement which was 0.22 *mm*.

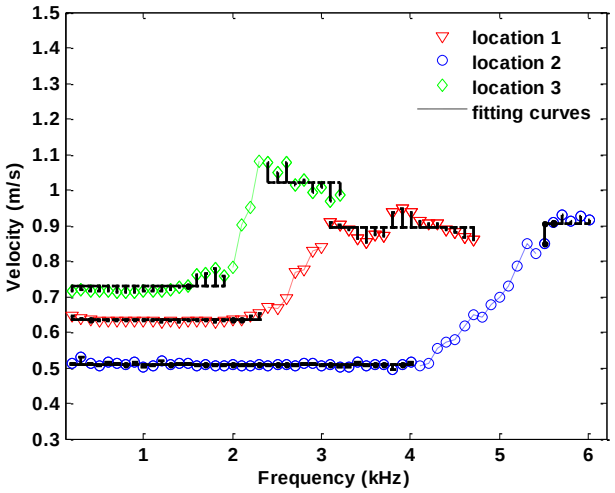

Figure 4- 18 Phase velocity of SAWs in an ex-vivo pig liver.

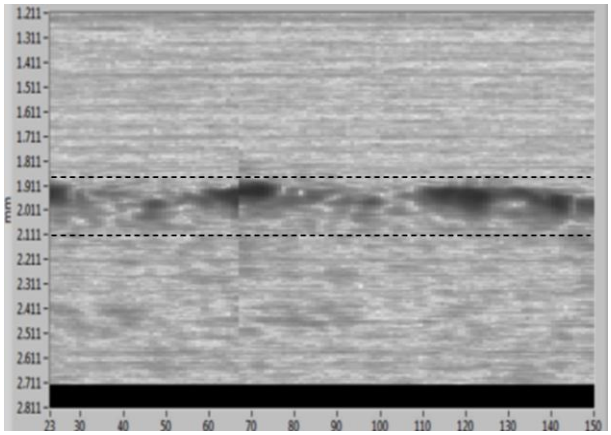

Figure 4- 19 High frequency ultrasound B-scan image showing the longitudinal-section of pig liver.

Table 4- 2 Mechanical properties of pig liver measured by SAWs phase velocity.

Liver	Phase velocity		Young's modulus		Dispersion centre frequency	Thickness
	tissue	Cuticle	tissue	cuticle		cuticle
Location 1	0.63	0.89	1.32	2.63	2.70	0.23
Location 2	0.51	0.92	0.86	2.81	4.81	0.11
Location 3	0.73	1.02	1.77	3.46	2.20	0.33
Average	0.62	0.94	1.32	2.97		0.22
Units	*m/s*		*kPa*		*kHz*	*mm*

4.5 Conclusion

In this chapter, the feasibility of tissue mechanical characterisation by SAWs was investigated by experiments. SAWs were generated by an electromagnetic shaker and detected by laser vibrometer. Experiments were conducted on different materials including homogeneous TMM phantoms, heterogeneous TMM phantoms and *ex-vivo* biological tissues. Results suggested that SAWs can be used to give a reliable mechanical characterisation of soft biological tissues, in terms of both stiffness quantification and the locating of stiffness boundaries. Phase velocity at low frequency reflected the stiffness of subtractive structure and phase velocity at high frequency characterised the stiffness of surface structure. The depth of the elasticity boundary can be estimated by the product of dispersion frequency and the mean phase velocity of subtractive layer.

Chapter 5 Conclusion and future work

5.1 Conclusion

The feasibility of using SAWs to sense and quantify the elasticity of tissue was studied in this dissertation from both modelling and experimental study.

In the FE simulation, SAWs were generated by a laser pulse in thermal elastic regime. Heat flux of laser was loaded on the model as thermal source, in which the temporal and spatial profile of laser pulse, optical absorption and scattering effect in tissue, and thermal diffusion were all accounted in. The model also includes a stiffer inclusion on the surface, leading to a stiffness alternation along both axial and lateral directions. Result shows that SAWs attenuation and group velocity are sensitive to the lateral elasticity change, and the phase velocity of SAWs is sensitive to the vertical elasticity change.

In tissue with lateral elasticity change along surface, SAWs attenuation increases dramatically at soft-to-hard boundary and decreases to negative at hard-to-soft boundary. This attenuation response can be utilised to locate elasticity boundaries along the tissue surface. Results also shows that SAWs propagate faster in hard tissue and spread slower in soft tissue, by substituting the SAWs group velocity into equation (4-3), elasticity of tissue can be quantified. For tissue with elasticity change at depth (multi-layer structure), SAWs phase velocity can be used to quantify the stiffness of each layer meantime can be also used to locate the boundary depth. Phase velocity at low frequencies characterise the stiffness of subtractive structure and phase velocity at high frequencies characterise the stiffness of surface structure. By dividing phase velocity of subtractive layer by the dispersion frequency, the depth of elasticity boundary can be estimated.

Results and supposes in simulation were then validated by experiments. SAWs were generated by electromagnetic shaker and detected by laser vibrometer. Homogeneous TMM phantoms with different stiffness were firstly been used to study the sensitivity and stability of our method. Result shows that stiffness measurement by SAWs has higher accuracy and smaller bias in soft TMM phantoms, and the sensitivity of SAWs measurement was high enough to identify a stiffness change of $5kPa$. An independent compression test of TMM phantoms was conducted to compare with and assess the elasticity measurement by SAWs.

Results show that the ratios of deviation between two methods were within 13%, indicated that mechanical characterisation by SAWs were reliable.

A two-layer TMM phantom with known surface-layer thickness was then used to validate SAWs mechanical characterisation of tissue with multi-layer structures. SAWs phase velocity was dispersed into two levels in the two-layer phantom. Young's modulus of surface layer was inversed from the phase velocity at low frequencies, and the Young's modulus of subtractive layer was inversed from the phase velocity of high frequencies. Young's modulus of each layer was comparable to the result in corresponding homogeneous phantoms, and the deviation ratio was within 15%. Surface layer thickness was also estimated by dividing phase velocity of subtractive layer by the dispersion frequency. Thickness measurement has a deviation of 0.19*mm* respect to the real value, with a deviation ratio of 3.6%. At last, SAWs measurement was conducted on an *ex-vivo* pig liver to validate the method in real biological tissue. The liver stiffness measured from SAWs matched to the published results, and the cuticle thickness measurement was validated by high frequency ultrasound imaging.

In summary, by using phase velocity of SAWs, this dissertation extended Zhang's work [8, 9] to mechanical characterisation of multi-layer structures. In the other hand, it also improved Li's work [13, 14] by making superficial layer thickness measurement.

5.2 Future work

In simulation, viscosity of tissue was not accounted in, which is apart from the situation in the reality. Therefore in further simulation studies viscosity attribute of tissue need to be considered in model. Also, model can be extended to three layers in the same thickness of epidermis, dermis, and subcutaneous fat of skin to simulate the realistic skin structures. SAWs phase velocity dispersion would be more complicated in this case and intense signal processing works are necessary for extracting the stiffness and thickness of each layer from the SAWs phase velocity dispersion. Meantime, blood vessels can be added into model to study the blood flow effect on SAWs and SAWs mechanical characterisation of skin.

In this dissertation, we only studied samples with vertical elasticity change in experiments. Therefore the first future work for experiment is to carry out experiments on samples with both lateral and vertical elasticity variation to validate the results of simulation. Besides, an optimization of current system could be the replacement of electromagnetic shaker to laser

generation of SAWs. Contact SAWs excitation methods are very sensitive to the geometry conditions and boundary conditions. For example, SAWs generation by electromagnetic shaker in our experiment is quite subject to the contact extent between shaker and sample. Robust SAWs can be generated only if shaker was carefully adjusted respect to the surface of sample. This would be even more difficult to achieve in the real clinical application as geometry of human skin can be much more complicated. Laser generation of SAWs is a non-contact mechanism which expects to eliminate the problems described above. Another advantage is that laser can be directed and generate SAWs within human body, which opened up the feasibility to characterize intern organs by our method. At last, the optical detection system in our experiment also needs to be optimized in the future, since the signal point laser vibrometer presented low signal to noise ratio (SNR) in scanning due to the insufficient optical reflection and scattering from sample surface. Once a more stable optical detection system is employed, SAWs can be generated in a fix location, and by scanning detection laser, elasticity mapping of skin can be achieved.

References

1. Rivaz H, Boctor EM, Choti MA, Hager GD: **Real-Time Regularized Ultrasound Elastography**. *Medical Imaging, IEEE Transactions on* 2011, **30**(4):928-945.
2. Uff CE, Garcia L, Fromageau J, Dorward N, Bamber JC: **Real-time ultrasound elastography in neurosurgery**. In: *Ultrasonics Symposium (IUS), 2009 IEEE International: 20-23 Sept. 2009 2009*. 467-470.
3. Zhu Q-L, Jiang Y-X, Liu J-B, Liu H, Sun Q, Dai Q, Chen X: **Real-Time Ultrasound Elastography: Its Potential Role in Assessment of Breast Lesions**. *Ultrasound in Medicine & Biology* 2008, **34**(8):1232-1238.
4. Palmeri ML, Nightingale KR: **Acoustic radiation force-based elasticity imaging methods**. *Interface Focus* 2011, **1**(4):553-564.
5. Nightingale K, McAleavey S, Trahey G: **Shear-wave generation using acoustic radiation force: in vivo and ex vivo results**. *Ultrasound in Medicine & Biology* 2003, **29**(12):1715-1723.
6. Wang H, et al.: **A three-dimensional quality-guided phase unwrapping method for MR elastography**. *Physics in Medicine and Biology* 2011, **56**(13):3935.
7. Mariappan YK, Glaser KJ, Hubmayr RD, Manduca A, Ehman RL, McGee KP: **MR elastography of human lung parenchyma: Technical development, theoretical modeling and in vivo validation**. *Journal of Magnetic Resonance Imaging* 2011, **33**(6):1351-1361.
8. Zhang X, Osborn TG, Pittelkow MR, Qiang B, Kinnick RR, Greenleaf JF: **Quantitative assessment of scleroderma by surface wave technique**. *Medical Engineering & Physics* 2011, **33**(1):31-37.
9. Zhang X, Greenleaf JF: **Estimation of tissue?s elasticity with surface wave speed**, vol. 122: ASA; 2007.
10. Catheline S, Gennisson J-L, Delon G, Fink M, Sinkus R, Abouelkaram S, Culioli J: **Measurement of viscoelastic properties of homogeneous soft solid using transient elastography: An inverse problem approach**, vol. 116: ASA; 2004.
11. Shigao C, Urban M, Pislaru C, Kinnick R, Yi Z, Aiping Y, Greenleaf J: **Shearwave dispersion ultrasound vibrometry (SDUV) for measuring tissue elasticity and viscosity**. *Ultrasonics, Ferroelectrics and Frequency Control, IEEE Transactions on* 2009, **56**(1):55-62.
12. Catheline S, Gennisson JL, Delon G, Fink M, Sinkus R, Abouelkaram S, Culioli J: **Measuring of viscoelastic properties of homogeneous soft solid using transient elastography: an inverse problem approach**. *The Journal of the Acoustical Society of America* 2004, **116**(6):3734-3741.
13. Li C, Huang Z, Wang RK: **Elastic properties of soft tissue-mimicking phantoms assessed by combined use of laser ultrasonics and low coherence interferometry**. *Opt Express* 2011, **19**(11):10153-10163.
14. Li C, Li S, Letang A, Huang Z, Wang R: **Finite element simulation of laser generated surface waves in layered skin model: effect of laser beam characteristics**, vol. 7898: SPIE; 2011.
15. Wells PNT, Liang H-D: **Medical ultrasound: imaging of soft tissue strain and elasticity**. *Journal of The Royal Society Interface* 2011.
16. Duck FA: **Physical properties of tissue.** . *London,UK: Academic Press* 1990.

17. Sarvazyan AP, Rudenko OV, Swanson SD, Fowlkes JB, Emelianov SY: **Shear wave elasticity imaging: a new ultrasonic technology of medical diagnostics**. *Ultrasound in Medicine & Biology* 1998, **24**(9):1419-1435.

18. Han L, Noble JA, Burche JA: **A novelultrasound indentation system for measuring the biomechanical properties of in vivo soft tissue**. *Ultrasound Med Biol* 2003, **29**:813-823.

19. Emelianov SY, Lubinski MA, Skovoroda AR, Erkamp RQ, Leavey SF, Wiggins RC, O'Donnell M: **Reconstructive ultrasound elasticity imaging for renal pathology detection**. In: *IEEE Ultrason Symp: 5–8 October 1997 1997; Toronto, Canada*. IEEE.: 1123 - 1126.

20. Egorov V, Tsyuryupa S, Kanilo S, Kogit M, Sarvazyan A: **Soft tissue elastometer**. *Med Eng Phys* 2008, **30**(206 - 212).

21. Krouskop TA, Wheeler TM, Kallel K, Garra BS, Hall T: **Elastic moduli of breast and prostate tissue under compression**. *Ultrason Imaging* 1998, **20**(260-274).

22. Sanada M: **Clinical evaluation of sonoelasticity measurement in liver using ultrasonic imaging of forced low-frequency vibration**. *Ultrasound Med Biol* 2000, **26**:1455-1460.

23. Samur E, Sedef, M., Basdogan, C., Avtan, L., Duzgun O: **A robotic indenter for minimally invasive measurement and characterization of soft tissue response**. *Med Imag Anal* 2007, **11**:361-373.

24. Samani A, Bishop J, Luginbuhl C, Plewes DB: **Measuring the elastic modulus of ex vivo small tissue samples**. *Phys Med Biol* 2003, **48**(2183-2198).

25. Parker KJ, Huang, S. R., Musulin, R. A. , Lerner RM: **Tissue response to mechanical vibrations for 'sonoelasticity imaging'**. *Ultrasound Med Biol* 1990, **16**:241-246.

26. Chen EJ, Novakofski, J., Jenkins, K., O'Brien,W.D.: **Young's modulus measurements of soft tissues with application to elasticity imaging**. *IEEE Trans UltrasonFerroelect Freq Contr* 1996, **43**:191-194.

27. Muller M, Gennisson, J. L., Deffieux, T., Tanter, M. , Fink M: **Quantitative viscoelasticity mapping of human liver using supersonic shear imaging: preliminary in vivo feasibility study**. *Ultrasound Med Biol* 2009, **35**:219-229.

28. Levinson SF, Shinagawa, M.,Sato, T. : **Sonoelastic determination of human skeletal muscle elasticity**. *J Biomech* 1995, **28**:1145-1154.

29. Yeh WC, Li, P. C., Jeng, Y. M., Hsu, H. C., Kuo, P. L.,, Li ML, Yang, P. M., Lee, P. H.: **Elastic modulus measurements of human liver and correlation with pathology**. *Ultrasound Med Biol* 2002, **28**:467-474.

30. Couade M, Pernot, M., Tanter, M., Messas, E., Bel, A., Ba,, M. Hg, A. A. ,Fink, M.: **Quantitative imaging of myocardium elasticity using supersonic shear imaging**. In: *IEEE Int Ultrason Symp: 20–23 September 2009 2009; Rome, Italy*. New York, NY: IEEE.: 151-154.

31. Xie H, al. e: **Correspondence of ultrasound elasticity imaging to direct mechanical measurement of aging in rats**. *Ultrasound Med Biol* 2005, **31**:1351-1359.

32. Ponnekanti H, Ophir J, Cespedes I: **Axial stress distributions between coaxial compressors in elastography: An analytical model**. *Ultrasound in Medicine & Biology* 1992, **18**(8):667-673.

33. Paul EB, Jeffrey CB: **Quantitative elasticity imaging: what can and cannot be inferred from strain images**. *Physics in Medicine and Biology* 2002, **47**(12):2147.

34. Lerner RM, Parker KJ: **Sonoelasticity imaging**. New York: Plenum Press; 1988.

35. Parker KJ, Huang SR, Musulin RA, Lerner RM: **Tissue response to mechanical vibrations for "sonoelasticity imaging"**. *Ultrasound in Medicine & Biology* 1990, **16**(3):241-246.

36. Lerner RM, Huang SR, Parker KJ: **"Sonoelasticity" images derived from ultrasound signals in mechanically vibrated tissues**. *Ultrasound in Medicine & Biology* 1990, **16**(3):231-239.

37. Taylor LS, et al.: **Three-dimensional sonoelastography: principles and practices**. *Physics in Medicine and Biology* 2000, **45**(6):1477.

38. Ophir J, Céspedes I, Ponnekanti H, Yazdi Y, Li X: **Elastography: A quantitative method for imaging the elasticity of biological tissues**. *Ultrasonic Imaging* 1991, **13**(2):111-134.

39. Shames I: **Mechanics of Deformable Solids**. Englewood Cliffs: Prentic-Hall; 1964.

40. Varghese T, Ophir J: **Estimating tissue strain from signal decorrelation using the correlation coefficient**. *Ultrasound in Medicine & Biology* 1996, **22**(9):1249-1254.

41. Srinivasan S, Ophir J: **A zero-crossing strain estimator for elastography**. *Ultrasound in Medicine & Biology* 2003, **29**(2):227-238.

42. Chen EJ, Novakofski J, Jenkins WK, O'Brien WD, Jr.: **Young's modulus measurements of soft tissues with application to elasticity imaging**. *Ultrasonics, Ferroelectrics and Frequency Control, IEEE Transactions on* 1996, **43**(1):191-194.

43. Huini D, Jie L, Pellot-Barakat C, Insana MF: **Optimizing multicompression approaches to elasticity imaging**. *Ultrasonics, Ferroelectrics and Frequency Control, IEEE Transactions on* 2006, **53**(1):90-99.

44. Lopata RGP, Nillesen MM, Hansen HHG, Gerrits IH, Thijssen JM, de Korte CL: **Performance Evaluation of Methods for Two-Dimensional Displacement and Strain Estimation Using Ultrasound Radio Frequency Data**. *Ultrasound in Medicine & Biology* 2009, **35**(5):796-812.

45. Skovoroda AR, Emelianov SY, Lubinski MA, Sarvazyan AP, O'Donnell M: **Theoretical analysis and verification of ultrasound displacement and strain imaging**. *Ultrasonics, Ferroelectrics and Frequency Control, IEEE Transactions on* 1994, **41**(3):302-313.

46. Skovoroda AR, Emelianov SY, O'Donnell M: **Tissue elasticity reconstruction based on ultrasonic displacement and strain images**. *Ultrasonics, Ferroelectrics and Frequency Control, IEEE Transactions on* 1995, **42**(4):747-765.

47. Skovoroda AR, Lubinski LA, Emelianov SY, O'Donnell M: **Reconstructive elasticity imaging for large deformations**. *Ultrasonics, Ferroelectrics and Frequency Control, IEEE Transactions on* 1999, **46**(3):523-535.

48. Torr G: **The acoustic radiation force**. *Am J Phys* 1984, **52**(5):402.

49. Sugimoto T, Ueha, S. , Itoh K: **Tissue hardness measurement using radiation force of focused ultrasound. In Proc.** . In: *IEEE Ultrason Symp: 4–7 December 1990 1990; Honolulu, HI*. NY: IEEE: 1377–1380.

50. Nightingale K, Soo MS, Nightingale R, Trahey G: **Acoustic radiation force impulse imaging: in vivo demonstration of clinical feasibility**. *Ultrasound in Medicine & Biology* 2002, **28**(2):227-235.

51. Melodelima D, Bamber JC, Duck FA, Shipley JA: **Transient Elastography Using Impulsive Ultrasound Radiation Force: A Preliminary Comparison With Surface Palpation Elastography**. *Ultrasound in Medicine & Biology* 2007, **33**(6):959-969.

52. Palmeri ML, Nightingale KR: **On the thermal effects associated with radiation force imaging of soft tissue**. *Ultrasonics, Ferroelectrics and Frequency Control, IEEE Transactions on* 2004, **51**(5):551-565.

53. Nightingale K, McAleavey S, Trahey G: **Shear-wave generation using acoustic radiation force: in vivo and ex vivo results**. *Ultrasound in Medicine & Biology* 2003, **29**(12):1715-1723.

54. Palmeri ML, Wang MH, Dahl JJ, Frinkley KD, Nightingale KR: **Quantifying Hepatic Shear Modulus In Vivo Using Acoustic Radiation Force**. *Ultrasound in Medicine & Biology* 2008, **34**(4):546-558.

55. Bercoff J, Tanter M, Fink M: **Supersonic shear imaging: a new technique for soft tissue elasticity mapping**. *Ultrasonics, Ferroelectrics and Frequency Control, IEEE Transactions on* 2004, **51**(4):396-409.

56. McAleavey SA, Menon, M. , Orszulak J: **Shear-modulus estimation by application of spatially-modulated impulsive acoustic radiation force**. *Ultrason Imaging* 2007, **29**:87-104

57. McAleavey SA, Menon, M. , Elege E: **Shear modulus imaging with spatially-modulated ultrasound radiation force.** *Ultrason Imaging* 2009, **31**:217–234.

58. Bercoff J, Tanter M, Muller M, Fink M: **The role of viscosity in the impulse diffraction field of elastic waves induced by the acoustic radiation force**. *Ultrasonics, Ferroelectrics and Frequency Control, IEEE Transactions on* 2004, **51**(11):1523-1536.

59. Van Houten EEW, Doyley MM, Kennedy FE, Weaver JB, Paulsen KD: **Initial in vivo experience with steady-state subzone-based MR elastography of the human breast**. *Journal of Magnetic Resonance Imaging* 2003, **17**(1):72-85.

60. Kemper J SR, Lorenzen J, Nolte-Ernsting C, Stork A , . AG: **MR elastography of the prostate:initial in-vivo application Rofo Fortschr**. *Geb Rontgenstr Neuen Bildgeb Verfahr* 2004, **176** 1094–1099.

61. Wu T, Felmlee JP, Greenleaf JF, Riederer SJ, Ehman RL: **MR imaging of shear waves generated by focused ultrasound**. *Magnetic Resonance in Medicine* 2000, **43**(1):111-115.

62. McCracken PJ, Manduca A, Felmlee J, Ehman RL: **Mechanical transient-based magnetic resonance elastography**. *Magnetic Resonance in Medicine* 2005, **53**(3):628-639.

63. Weaver JB, Doyley M, Cheung Y, Kennedy F, Madsen EL, Van Houten EEW, Paulsen K: **Imaging the shear modulus of the heel fat pads**. *Clinical Biomechanics* 2005, **20**(3):312-319.

64. Schmitt JM: **OCT elastography: imaging microscopic deformation and strain of tissue** *Opt Express* 1998, **3**(199–211).

65. Kirkpatrick SJ, Wang RK, Duncan DD: **OCT-based elastography for large and small deformations**. *Opt Express* 2006, **14**(24):11585-11597.

66. Kennedy BF, Hillman TR, McLaughlin RA, Quirk BC, Sampson DD: **In vivo dynamic optical coherence elastography using a ring actuator**. *Opt Express* 2009, **17**(24):21762-21772.

67. Miller GF, Pursey H: **The Field and Radiation Impedance of Mechanical Radiators on the Free Surface of a Semi-Infinite Isotropic Solid**. *Proceedings of the Royal Society of London Series A Mathematical and Physical Sciences* 1954, **223**(1155):521-541.

68. Daniel N: **A new formula for the velocity of Rayleigh waves**. *Wave Motion* 1997, **26**(2):199-205.

69. Royer D, Clorennec D: **An improved approximation for the Rayleigh wave equation**. *Ultrasonics* 2007, **46**(1):23-24.

70. Viktorov IA: **Rayleigh and Lamb waves: Physical theory and applications** *Plenum Press (New York)* 1967 **QC244 .V513**.

71. ed.org/EducationResources ErftNrchwn-.

72. Jian X, Dixon S, Grattan KTV, Edwards RS: **A model for pulsed Rayleigh wave and optimal EMAT design**. *Sensors and Actuators A: Physical* 2006, **128**(2):296-304.

73. E.R. Dobbs WPM, R.N. Thurston: **Electromagnetic Generation of Ultrasonic Waves Physical Acoustics***Academic Press* 1973, **vol. 10 p. 127**:p. 127.

74. Ludwig R, You Z, Palanisamy R: **Numerical simulations of an electromagnetic acoustic transducer-receiver system for NDT applications**. *Magnetics, IEEE Transactions on* 1993, **29**(3):2081-2089.

75. Jian X, Dixon S, Edwards RS, Morrison J: **Coupling mechanism of an EMAT**. *Ultrasonics* 2006, **44, Supplement**(0):e653-e656.

76. Baldwin DWBaKC: **Laser-Based Ultrasonics: Applications at APL**. *Johns Hopkins APL Technical Digest* 2005, **26**(1).

77. Sorazu B, Thursby G, Culshaw B, Dong F, Pierce SG, Yang Y, Betz D: **Optical Generation and Detection of Ultrasound**. *Strain* 2003, **39**(3):111-114.

78. L'Etang AJ: **Development of a Novel Laser-Ultrasonic** *PHD thesis (UoD)* 2009.

79. Sohn Y, Krishnaswamy S: **Mass spring lattice modeling of the scanning laser source technique**. *Ultrasonics* 2002, **39**(8):543-551.

80. Neubrand A, Hess P: **Laser generation and detection of surface acoustic waves: Elastic properties of surface layers**. *Journal of Applied Physics* 1992, **71**(1):227-238.

81. Schneider D, Schwarz T: **A photoacoustic method for characterising thin films**. *Surface and Coatings Technology* 1997, **91**(1-2):136-146.

82. Xu B, Shen Z, Ni X, Lu J: **Numerical simulation of laser-generated ultrasound by the finite element method**. *Journal of Applied Physics* 2004, **95**(4):2116-2122.

83. Xu B, Shen Z, Ni X, Lu J, Wang Y: **Finite element model of laser-generated surface acoustic waves in coating-substrate system**. *Journal of Applied Physics* 2004, **95**(4):2109-2115.

84. Wang J, Shen Z, Xu B, Ni X, Guan J, Lu J: **Numerical simulation of laser-generated ultrasound in non-metallic material by the finite element method**. *Optics & Laser Technology* 2007, **39**(4):806-813.

85. User manual of OFV-534 Laser vibrometer, Polytec, http://www.polytec-ltd.co.uk/.

Appendix A

Codes in ANSYS

```
finish
/clear
/FILNAM,Two_h_1!
/TITLE,S_H_S!
/UNITS,SI!
/PREP7
ET,1,PLANE55

KEYOPT,1,1,0
KEYOPT,1,3,1
KEYOPT,1,4,0
KEYOPT,1,8,0
KEYOPT,1,9,0

RECTNG,0,1.5e-3,0,-0.5e-3,
RECTNG,1.5e-3,4e-3,0,-0.5e-3,
RECTNG,4e-3,6.5e-3,0,-0.5e-3,
RECTNG,6.5e-3,9e-3,0,-0.5e-3,

RECTNG,0,1.5e-3,-0.5e-3,-2e-3,
RECTNG,1.5e-3,4e-3,-0.5e-3,-2e-3,
RECTNG,4e-3,6.5e-3,-0.5e-3,-2e-3,
RECTNG,6.5e-3,9e-3,-0.5e-3,-2e-3,

RECTNG,0,1.5e-3,-2e-3,-5e-3,
RECTNG,1.5e-3,4e-3,-2e-3,-5e-3,
RECTNG,4e-3,6.5e-3,-2e-3,-5e-3,
RECTNG,6.5e-3,9e-3,-2e-3,-5e-3,

RECTNG,0,1.5e-3,-5e-3,-10e-3,
RECTNG,1.5e-3,4e-3,-5e-3,-10e-3,
RECTNG,4e-3,6.5e-3,-5e-3,-10e-3,
RECTNG,6.5e-3,9e-3,-5e-3,-10e-3,

FLST,2,16,5,ORDE,2
FITEM,2,1
FITEM,2,-16
AGLUE,P51X

!* Material property

!* soft material

MPTEMP,,,,,,,,
MPTEMP,1,0
UIMP,1,REFT,,,

MPDATA,DENS,1,,1060
MPTEMP,,,,,,,,
MPTEMP,1,0
```

```
MPDATA,EX,1,,87097
MPDATA,PRXY,1,,0.49
MPTEMP,,,,,,,,
MPTEMP,1,0

MPDATA,ALPX,1,,3e-4
MPTEMP,,,,,,,,
MPTEMP,1,0

MPDATA,KXX,1,,0.45
MPTEMP,,,,,,,,
MPTEMP,1,0

MPDATA,C,1,,3300

!* Hard material

MPTEMP,,,,,,,,
MPTEMP,1,0
UIMP,2,REFT,,,

MPDATA,DENS,2,,1080
MPTEMP,,,,,,,,
MPTEMP,1,0

MPDATA,EX,2,,1.36e5
MPDATA,PRXY,2,,0.49
MPTEMP,,,,,,,,
MPTEMP,1,0

MPDATA,ALPX,2,,3e-4
MPTEMP,,,,,,,,
MPTEMP,1,0

MPDATA,KXX,2,,0.45
MPTEMP,,,,,,,,
MPTEMP,1,0

MPDATA,C,2,,3300

!* Hardest material

MPTEMP,,,,,,,,
MPTEMP,1,0
UIMP,3,REFT,,,

MPDATA,DENS,3,,1100
MPTEMP,,,,,,,,
MPTEMP,1,0

MPDATA,EX,3,,511147.4
MPDATA,PRXY,3,,0.49
MPTEMP,,,,,,,,
MPTEMP,1,0
```

```
MPDATA,ALPX,3,,3e-4
MPTEMP,,,,,,,,
MPTEMP,1,0

MPDATA,KXX,3,,0.45
MPTEMP,,,,,,,,
MPTEMP,1,0

MPDATA,C,3,,3300

!*  MESH!

!* Mesh attibutes!

!* up-left

FLST,5,4,5,ORDE,4
FITEM,5,1
FITEM,5,17
FITEM,5,-18
FITEM,5,23
CM,_Y,AREA
ASEL, , , ,P51X
CM,_Y1,AREA
CMSEL,S,_Y
!*
CMSEL,S,_Y1
AATT,      1, ,   1,      0,
CMSEL,S,_Y
CMDELE,_Y
CMDELE,_Y1

!* up-mid

FLST,5,2,5,ORDE,2
FITEM,5,19
FITEM,5,24
CM,_Y,AREA
ASEL, , , ,P51X
CM,_Y1,AREA
CMSEL,S,_Y
!*
CMSEL,S,_Y1
AATT,      3, ,   1,      0,
CMSEL,S,_Y
CMDELE,_Y
CMDELE,_Y1

!* up-right

FLST,5,2,5,ORDE,2
FITEM,5,20
FITEM,5,25
CM,_Y,AREA
```

```
ASEL, , , ,P51X
CM,_Y1,AREA
CMSEL,S,_Y
!*
CMSEL,S,_Y1
AATT,      1, ,   1,      0,
CMSEL,S,_Y
CMDELE,_Y
CMDELE,_Y1

!* down-left

FLST,5,4,5,ORDE,4
FITEM,5,21
FITEM,5,-22
FITEM,5,26
FITEM,5,29
CM,_Y,AREA
ASEL, , , ,P51X
CM,_Y1,AREA
CMSEL,S,_Y
!*
CMSEL,S,_Y1
AATT,      1, ,   1,      0,
CMSEL,S,_Y
CMDELE,_Y
CMDELE,_Y1

!* down-mid

FLST,5,2,5,ORDE,2
FITEM,5,27
FITEM,5,30
CM,_Y,AREA
ASEL, , , ,P51X
CM,_Y1,AREA
CMSEL,S,_Y
!*
CMSEL,S,_Y1
AATT,      1, ,   1,      0,
CMSEL,S,_Y
CMDELE,_Y
CMDELE,_Y1

!* down-right

FLST,5,2,5,ORDE,2
FITEM,5,28
FITEM,5,31
CM,_Y,AREA
ASEL, , , ,P51X
CM,_Y1,AREA
CMSEL,S,_Y
CMSEL,S,_Y1
AATT,      1, ,   1,      0,
```

```
CMSEL,S,_Y
CMDELE,_Y
CMDELE,_Y1

!*   Mesh line size!

FLST,5,3,4,ORDE,2
FITEM,5,2
FITEM,5,-4
CM,_Y,LINE
LSEL, , , ,P51X
CM,_Y1,LINE
CMSEL,,_Y
!*
LESIZE,_Y1,5e-6, , , , , , ,1
!*
FLST,5,3,4,ORDE,3
FITEM,5,68
FITEM,5,70
FITEM,5,72
CM,_Y,LINE
LSEL, , , ,P51X
CM,_Y1,LINE
CMSEL,,_Y
!*
LESIZE,_Y1,10e-006, , , , , , ,1
!*
FLST,5,2,4,ORDE,2
FITEM,5,6
FITEM,5,10
CM,_Y,LINE
LSEL, , , ,P51X
CM,_Y1,LINE
CMSEL,,_Y
!*
LESIZE,_Y1,1.5e-005, , , , , , ,1
!*
FLST,5,5,4,ORDE,5
FITEM,5,1
FITEM,5,14
FITEM,5,67
FITEM,5,69
FITEM,5,71
CM,_Y,LINE
LSEL, , , ,P51X
CM,_Y1,LINE
CMSEL,,_Y
!*
LESIZE,_Y1,2e-005, , , , , , ,1
!*
FLST,5,1,4,ORDE,1
FITEM,5,65
CM,_Y,LINE
LSEL, , , ,P51X
CM,_Y1,LINE
```

```
CMSEL,,_Y
!*
LESIZE,_Y1,4e-005, , , , , ,1
!*
FLST,5,3,4,ORDE,3
FITEM,5,66
FITEM,5,77
FITEM,5,79
CM,_Y,LINE
LSEL, , , ,P51X
CM,_Y1,LINE
CMSEL,,_Y
!*
LESIZE,_Y1,5e-005, , , , , ,1
!*
FLST,5,5,4,ORDE,4
FITEM,5,17
FITEM,5,78
FITEM,5,80
FITEM,5,-82
CM,_Y,LINE
LSEL, , , ,P51X
CM,_Y1,LINE
CMSEL,,_Y
!*
LESIZE,_Y1,10e-005, , , , , ,1
!*
FLST,5,1,4,ORDE,1
FITEM,5,73
CM,_Y,LINE
LSEL, , , ,P51X
CM,_Y1,LINE
CMSEL,,_Y
!*
LESIZE,_Y1,0.0001, , , , , ,1
!*
FLST,5,3,4,ORDE,3
FITEM,5,74
FITEM,5,83
FITEM,5,85
CM,_Y,LINE
LSEL, , , ,P51X
CM,_Y1,LINE
CMSEL,,_Y
!*
LESIZE,_Y1,0.00015, , , , , ,1
!*
FLST,5,5,4,ORDE,4
FITEM,5,33
FITEM,5,84
FITEM,5,86
FITEM,5,-88
CM,_Y,LINE
LSEL, , , ,P51X
CM,_Y1,LINE
```

```
CMSEL,,_Y
!*
LESIZE,_Y1,0.00025, , , , , ,1
!*
FLST,5,1,4,ORDE,1
FITEM,5,75
CM,_Y,LINE
LSEL, , , ,P51X
CM,_Y1,LINE
CMSEL,,_Y
!*
LESIZE,_Y1,0.0002, , , , , ,1
!*
FLST,5,3,4,ORDE,3
FITEM,5,76
FITEM,5,89
FITEM,5,91
CM,_Y,LINE
LSEL, , , ,P51X
CM,_Y1,LINE
CMSEL,,_Y
!*
LESIZE,_Y1,0.0003, , , , , ,1
!*
FLST,5,5,4,ORDE,4
FITEM,5,49
FITEM,5,90
FITEM,5,92
FITEM,5,-94
CM,_Y,LINE
LSEL, , , ,P51X
CM,_Y1,LINE
CMSEL,,_Y
!*
LESIZE,_Y1,0.0005, , , , , ,1
!*
MSHAPE,0,2D
MSHKEY,1
!*
FLST,5,16,5,ORDE,3
FITEM,5,1
FITEM,5,17
FITEM,5,-31
CM,_Y,AREA
ASEL, , , ,P51X
CM,_Y1,AREA
CHKMSH,'AREA'
CMSEL,S,_Y
!*
AMESH,_Y1
!*
CMDELE,_Y
CMDELE,_Y1
CMDELE,_Y2
!*
```

```
!* SOLUSTION!
!* SOLU CONTROL!

/SOL
ANTYPE,4
TRNOPT,FULL
LUMPM,0

NSUBST,1000,0,0
OUTRES,ERASE
OUTRES,NSOL,ALL
AUTOTS,0
TIME,10000e-9

!* UNIF TEM!

TUNIF,300,

!* FUNCTION!
*DEL,_FNCNAME
*DEL,_FNCMTID
*DEL,_FNC_C1
*DEL,_FNC_C2
*DEL,_FNC_C3
*DEL,_FNC_C4
*DEL,_FNCCSYS
*SET,_FNCNAME,'tissue'
*DIM,_FNC_C1,,1
*DIM,_FNC_C2,,1
*DIM,_FNC_C3,,1
*DIM,_FNC_C4,,1
*SET,_FNC_C1(1),86000
*SET,_FNC_C2(1),2e-3
*SET,_FNC_C3(1),0.5e-3
*SET,_FNC_C4(1),10e-9
*SET,_FNCCSYS,0
! /INPUT,tissue.func,,,1
*DIM,%_FNCNAME%,TABLE,6,35,1,,,,%_FNCCSYS%
!
! Begin of equation: U*(2*W/({PI}*(R)^2*T))*exp(-2*({X}^2/R^2))*exp(U*{Y})*
! ({TIME}/T)*exp(-{TIME}/T)
! End of equation: U*(2*W/({PI}*(R)^2*T))*exp(-2*({X}^2/R^2))*exp(U*{Y})*
! ({TIME}/T)*exp(-{TIME}/T)
!-->
!* SELECT ENTITY!
NSEL,S,LOC,Y,0,-0.012e-3

!* APPLY HEAT!
FLST,2,3153,1,ORDE,2104
/GO
!*
BF,P51X,HGEN, %TISSUE%  !* SOLVE!
```

Appendix B

Codes in Matlab for signal processing

```
close all;
clear all;

mypath='C:\Documents and Settings\STLi-P\My Documents\MATLAB\liver
processed data\';

n1=2;
m1=60;

v_1=csvread([mypath,'liver_1_2.txt']);
v_1=v_1(n1:m1);
f_1=csvread([mypath,'fselect_liver_1_2.txt']);
f_1=f_1(n1:m1);

mean_v_1=mean(v_1);

n2=2;
m2=60;

v_2=csvread([mypath,'liver_2_2.txt']);
v_2=v_2(n2:m2);
f_2=csvread([mypath,'fselect_liver_2_2.txt']);
f_2=f_2(n2:m2);

mean_v_2=mean(v_2);

n3=2;
m3=60;

v_3=csvread([mypath,'liver_3_2.txt']);
v_3=v_3(n3:m3);
f_3=csvread([mypath,'fselect_liver_3_2.txt']);
f_3=f_3(n3:m3);

mean_v_3=mean(v_3);

v=(v_1+v_2+v_3)/3;
I=[v_1 v_2 v_3];

mean_v=mean(v);

Max=max(I,[],2);
high=Max-v;
Min=min(I,[],2);
low=Min-v;

NFFT=length(f_1);

%%%
```

```
fmin=100;
fmax=index_1;

A=[];
for n=1:NFFT
    if fmin<=f_1(n)
       if fmax>=f_1(n)
            a=n;
            A=[A,a];

        end
    end
end

phase_velocity=v_1(A(1):A(length(A)));
fselected=f_1(A(1):A(length(A)));

mean_velocity=mean(phase_velocity);
V1=num2str(mean_velocity);

MEAN=ones(length(A),1);
MEAN=MEAN*mean_velocity;

H_or_L=phase_velocity-MEAN;
H=[];
L=[];

for n=1:length(H_or_L)
    if H_or_L(n)>0
        H(n)=H_or_L(n);
        L(n)=0;
    else
        L(n)=H_or_L(n);
        H(n)=0;
    end
end

% figure
% f1=polyfit(fselected,phase_velocity,1);
% ca=f1(1)*fselected+f1(2);
% figure

% plot(fselected/1000,phase_velocity,'vr');
% hold on;

% plot(fselected/1000,ca,'k--');
% hold on;

% figure
%
% plot(fselected/1000,phase_velocity,'vr','linewidth',0.5);
% h1=plot(fselected/1000,phase_velocity,'vr','linewidth',0.5);
%
% hold on;
% plot(fselected/1000,MEAN,'k--');
% h2=plot(fselected/1000,MEAN,'k--');
% hold on;
```

```
figure

plot(fselected/1000,phase_velocity,'vr','linewidth',0.5);
h1=plot(fselected/1000,phase_velocity,'vr','linewidth',0.5);

hold on;
errorbar(fselected/1000,MEAN,L,H,'k--');
h2=errorbar(fselected/1000,MEAN,L,H,'k--');
hold on;


fmin=index_2;
fmax=4800;

A=[];
for n=1:NFFT
    if fmin<=f_1(n)
       if fmax>=f_1(n)
            a=n;
            A=[A,a];

        end
    end
end

phase_velocity=v_1(A(1):A(length(A)));
fselected=f_1(A(1):A(length(A)));

mean_velocity=mean(phase_velocity);
V2=num2str(mean_velocity);

MEAN=ones(length(A),1);
MEAN=MEAN*mean_velocity;

H_or_L=phase_velocity-MEAN;
H=[];
L=[];

for n=1:length(H_or_L)
    if H_or_L(n)>0
        H(n)=H_or_L(n);
        L(n)=0;
    else
        L(n)=H_or_L(n);
        H(n)=0;
    end
end


% f1=polyfit(fselected,phase_velocity,1);
% ca=f1(1)*fselected+f1(2);
% figure

% plot(fselected/1000,phase_velocity,'vr');
% hold on;

% plot(fselected/1000,ca,'k--');
% hold on;
```

```
% plot(fselected/1000,phase_velocity,'vr','linewidth',0.5);
% h1=plot(fselected/1000,phase_velocity,'vr','linewidth',0.5);
%
% hold on;
% plot(fselected/1000,MEAN,'k--');
% h2=plot(fselected/1000,MEAN,'k--');
% hold on;



plot(fselected/1000,phase_velocity,'vr','linewidth',0.5);
h1=plot(fselected/1000,phase_velocity,'vr','linewidth',0.5);

hold on;
errorbar(fselected/1000,MEAN,L,H,'k--');
h2=errorbar(fselected/1000,MEAN,L,H,'k--');
hold on;


fmin=index_1;
fmax=index_2;

A=[];
for n=1:NFFT
    if fmin<=f_1(n)
       if fmax>=f_1(n)
            a=n;
            A=[A,a];

        end
    end
end

phase_velocity=v_1(A(1):A(length(A)));
fselected=f_1(A(1):A(length(A)));


plot(fselected/1000,phase_velocity,'vr','linewidth',0.5,'MarkerSize',7);
hold on;


%%%%%%%%%%%%%%%%%%%%%%%%%%%%%%%%%%%%%%%%%%%%%%%%%%%%%%%%%%%%%%%%%%%%%%%%%%%%%%%%
%%%%%%%%%%%%%%%%%%%%%%%%%%%%%%%%%%%%%%%%%%%%%%%%%%%%%%%%%%%%%%%%%%%%%%%%%%%%%%%%

index_1=4100;
index_2=5500;

fmin=100;
fmax=index_1;

A=[];
for n=1:NFFT
    if fmin<=f_2(n)
       if fmax>=f_2(n)
```

```
            a=n;
            A=[A,a];

        end
    end
end

phase_velocity=v_2(A(1):A(length(A)));
fselected=f_2(A(1):A(length(A)));

mean_velocity=mean(phase_velocity);
V3=num2str(mean_velocity);

MEAN=ones(length(A),1);
MEAN=MEAN*mean_velocity;

H_or_L=phase_velocity-MEAN;
H=[];
L=[];

for n=1:length(H_or_L)
    if H_or_L(n)>0
        H(n)=H_or_L(n);
        L(n)=0;
    else
        L(n)=H_or_L(n);
        H(n)=0;
    end
end

% figure
% f1=polyfit(fselected,phase_velocity,1);
% ca=f1(1)*fselected+f1(2);
% figure

% plot(fselected/1000,phase_velocity,'vr');
% hold on;

% plot(fselected/1000,ca,'k--');
% hold on;



% plot(fselected/1000,phase_velocity,'ob','linewidth',0.5);
% h3=plot(fselected/1000,phase_velocity,'ob','linewidth',0.5);
%
% hold on;
% plot(fselected/1000,MEAN,'k--');
% h4=plot(fselected/1000,MEAN,'k--');
% hold on;


plot(fselected/1000,phase_velocity,'ob','linewidth',0.5);
h3=plot(fselected/1000,phase_velocity,'ob','linewidth',0.5);

hold on;
errorbar(fselected/1000,MEAN,L,H,'k--');
h4=errorbar(fselected/1000,MEAN,L,H,'k--');
```

```
hold on;


fmin=index_2;
fmax=6500;

A=[];
for n=1:NFFT
    if fmin<=f_2(n)
       if fmax>=f_2(n)
            a=n;
            A=[A,a];

        end
    end
end

phase_velocity=v_2(A(1):A(length(A)));
fselected=f_2(A(1):A(length(A)));

mean_velocity=mean(phase_velocity);
V4=num2str(mean_velocity);

MEAN=ones(length(A),1);
MEAN=MEAN*mean_velocity;

H_or_L=phase_velocity-MEAN;
H=[];
L=[];

for n=1:length(H_or_L)
    if H_or_L(n)>0
        H(n)=H_or_L(n);
        L(n)=0;
    else
        L(n)=H_or_L(n);
        H(n)=0;
    end
end

% figure
% f1=polyfit(fselected,phase_velocity,1);
% ca=f1(1)*fselected+f1(2);
% figure

% plot(fselected/1000,phase_velocity,'vr:','linewidth',0.5);
% hold on;

% plot(fselected/1000,ca,'k--');
% hold on;


% plot(fselected/1000,phase_velocity,'ob','linewidth',0.5);
% h3=plot(fselected/1000,phase_velocity,'ob','linewidth',0.5);
%
% hold on;
% plot(fselected/1000,MEAN,'k--');
% h4=plot(fselected/1000,MEAN,'k--');
```

```
% hold on;


plot(fselected/1000,phase_velocity,'ob','linewidth',0.5);
h3=plot(fselected/1000,phase_velocity,'ob','linewidth',0.5);

hold on;
errorbar(fselected/1000,MEAN,L,H,'k--');
h4=errorbar(fselected/1000,MEAN,L,H,'k--');
hold on;


fmin=index_1;
fmax=index_2;

A=[];
for n=1:NFFT
    if fmin<=f_2(n)
       if fmax>=f_2(n)
            a=n;
            A=[A,a];

        end
    end
end

phase_velocity=v_2(A(1):A(length(A)));
fselected=f_2(A(1):A(length(A)));


plot(fselected/1000,phase_velocity,'ob','linewidth',0.5,'MarkerSize',7);

%%%%%%%%%%%%%%%%%%%%%%%%%%%%%%%%%%%%%%%%%%%%%%%%%%%%%%%%%%%%%%%%%%%%%%%%%%%%%%%
%%%%%%%%%%%%%%%%%%%%%%%%%%%%%%%%%%%%%%%%%%%%%%%%%%%%%%%%%%%%%%%%%%%%%%%%%%%%%%%

index_1=2000;
index_2=2400;

fmin=100;
fmax=index_1;

A=[];
for n=1:NFFT
    if fmin<=f_3(n)
       if fmax>=f_3(n)
            a=n;
            A=[A,a];

        end
    end
end

phase_velocity=v_3(A(1):A(length(A)));
fselected=f_3(A(1):A(length(A)));

mean_velocity=mean(phase_velocity);
V5=num2str(mean_velocity);
```

```
MEAN=ones(length(A),1);
MEAN=MEAN*mean_velocity;

H_or_L=phase_velocity-MEAN;
H=[];
L=[];

for n=1:length(H_or_L)
    if H_or_L(n)>0
        H(n)=H_or_L(n);
        L(n)=0;
    else
        L(n)=H_or_L(n);
        H(n)=0;
    end
end

% figure
% f1=polyfit(fselected,phase_velocity,1);
% ca=f1(1)*fselected+f1(2);
% figure
% set(0,'DefaultLineLineWidth',2);
% plot(fselected/1000,phase_velocity,'vr:');
% hold on;
% set(0,'DefaultLineLineWidth',2);
% plot(fselected/1000,ca,'k--');
% hold on;



% plot(fselected/1000,phase_velocity,'diamondg','linewidth',0.5);
% h5=plot(fselected/1000,phase_velocity,'diamondg','linewidth',0.5);
% hold on;
% plot(fselected/1000,MEAN,'k--');
% h6=plot(fselected/1000,MEAN,'k--');
% hold on;


plot(fselected/1000,phase_velocity,'diamondg','linewidth',0.5);
h5=plot(fselected/1000,phase_velocity,'diamondg','linewidth',0.5);
hold on;
errorbar(fselected/1000,MEAN,L,H,'k--');
h6=errorbar(fselected/1000,MEAN,L,H,'k--');
hold on;


fmin=index_2;
fmax=3300;

A=[];
for n=1:NFFT
    if fmin<=f_3(n)
       if fmax>=f_3(n)
            a=n;
            A=[A,a];

        end
    end
end
```

```
phase_velocity=v_3(A(1):A(length(A)));
fselected=f_3(A(1):A(length(A)));

mean_velocity=mean(phase_velocity);
V6=num2str(mean_velocity);

MEAN=ones(length(A),1);
MEAN=MEAN*mean_velocity;

H_or_L=phase_velocity-MEAN;
H=[];
L=[];

for n=1:length(H_or_L)
    if H_or_L(n)>0
        H(n)=H_or_L(n);
        L(n)=0;
    else
        L(n)=H_or_L(n);
        H(n)=0;
    end
end

% figure
% f1=polyfit(fselected,phase_velocity,1);
% ca=f1(1)*fselected+f1(2);
% figure

% plot(fselected/1000,phase_velocity,'vr:');
% hold on;

% plot(fselected/1000,ca,'k--');
% hold on;



% plot(fselected/1000,phase_velocity,'diamondg','linewidth',0.5);
% h5=plot(fselected/1000,phase_velocity,'diamondg','linewidth',0.5);
%
% hold on;
% plot(fselected/1000,MEAN,'k--');
% h6=plot(fselected/1000,MEAN,'k--');
% hold on;


plot(fselected/1000,phase_velocity,'diamondg','linewidth',0.5);
h5=plot(fselected/1000,phase_velocity,'diamondg','linewidth',0.5);

hold on;
errorbar(fselected/1000,MEAN,L,H,'k--');
h6=errorbar(fselected/1000,MEAN,L,H,'k--');
hold on;


fmin=index_1;
fmax=index_2;
```

```
A=[];
for n=1:NFFT
    if fmin<=f_3(n)
       if fmax>=f_3(n)
            a=n;
            A=[A,a];

        end
    end
end

phase_velocity=v_3(A(1):A(length(A)));
fselected=f_3(A(1):A(length(A)));


plot(fselected/1000,phase_velocity,'diamondg','linewidth',0.5,'MarkerSize',
7);
hold on;


xlabel('Frequency (kHz)','fontsize',12,'FontWeight','demi');
ylabel('Velocity (m/s)','fontsize',12,'FontWeight','demi');
set(gca, 'YLim',[0.2 2]);
set(gca, 'XLim',[0.12 6.2]);
set(gca,'fontsize',12,'FontWeight','demi');

legend([h1,h3,h5,h2],'location 1','location 2','location 3','fitting
curves');
set(legend,'fontsize',12,'FontWeight','demi');
legend('boxoff');

gtext([V1,'m/s '],'fontsize',10,'FontWeight','demi');
gtext([V2,'m/s '],'fontsize',10,'FontWeight','demi');
gtext([V3,'m/s '],'fontsize',10,'FontWeight','demi');
gtext([V4,'m/s '],'fontsize',10,'FontWeight','demi');
gtext([V5,'m/s '],'fontsize',10,'FontWeight','demi');
gtext([V6,'m/s '],'fontsize',10,'FontWeight','demi');

%%%%%%%%%%%%%%%%%%%%%%%%%%%%%%%%%%%%%%%%%%%%%%%%%%%%%%%%%%%%%%%%%%%%%%%%%%%%
%%%%%%%%%%%%%%%%%%%%%%%%%%%%%%%%%%%%%%%%%%%%%%%%%%%%%%%%%%%%%%%%%%%%%%%%%%%%

figure

% errorbar(f_1/1000,v_1,low_1,high_1,'ob-');
% hold on;
% errorbar(f_2/1000,v_2,low_2,high_2,'or--');
% hold on;
% errorbar(f_3/1000,v_3,low_3,high_3,'og:');

% errorbar(f_3/1000,v,low,high,'ob:');

set(0,'DefaultLineLineWidth',2);

plot(f_1/1000,v_1,'ob-');
hold on;
plot(f_2/1000,v_2,'*r--');
hold on;
plot(f_3/1000,v_3,'^g:');
```

```
% title('Phase velocity on agar
phantoms','fontsize',12,'FontWeight','bold');
xlabel('Frequency (kHz)','fontsize',12,'FontWeight','bold');
ylabel('Velocity (m/s)','fontsize',12,'FontWeight','bold');
set(gca, 'YLim',[0 5]);
set(gca, 'XLim',[0.12 6.2]);
% legend('Phase velocity of SAWs on liver 1', 1,'Phase velocity of SAWs on
liver 2',2, 'Phase velocity of SAWs on liver 3',3);
legend('Stastics analysis of SAWs phase velocity on diffirent pig livers ',
1);

V3=num2str(mean_v_3);
V2=num2str(mean_v_2);
V1=num2str(mean_v_1);
V=num2str(mean_v);
% gtext(['V(liver 1) = ',V1,'m/s; ','V(liver 2) = ',V2,'m/s; ','V(liver 3)
= ',V3,'m/s; ']);
% gtext(['Phase velocity on pig liver (average) = ',V,'m/s']);

% subplot(2,1,2)
% % plot(f/1000,h1,'ob');
% % hold on;
% plot(f/1000,h,'o');
% title('Detection depth on liver','fontsize',12,'FontWeight','bold');
% xlabel('Frequency (kHz)','fontsize',11,'FontWeight','bold');
% ylabel('Depth (mm)','fontsize',11,'FontWeight','bold');
% % Dlow1=num2str(h1(1));
% % Dhigh1=num2str(h1(length(h1)));
% Dlow2=num2str(h(1));
% Dhigh2=num2str(h(length(h)));
% gtext(['Characterisation depth from ',Dhigh2,' mm',' to ',Dlow2,' mm']);
%
% % gtext(['Depth range(2%) from ',Dhigh1,' mm',' to ',Dlow1,' mm','Depth
range(3%) from ',Dhigh2,' mm',' to ',Dlow2,' mm']);
%
%
```

Appendix C

Labview front panel of robotic communication

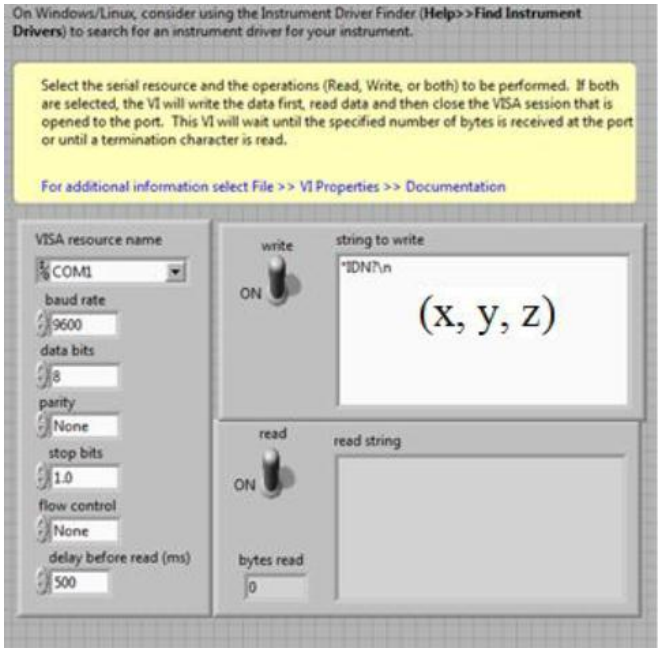

Labview back panel of robotic communication

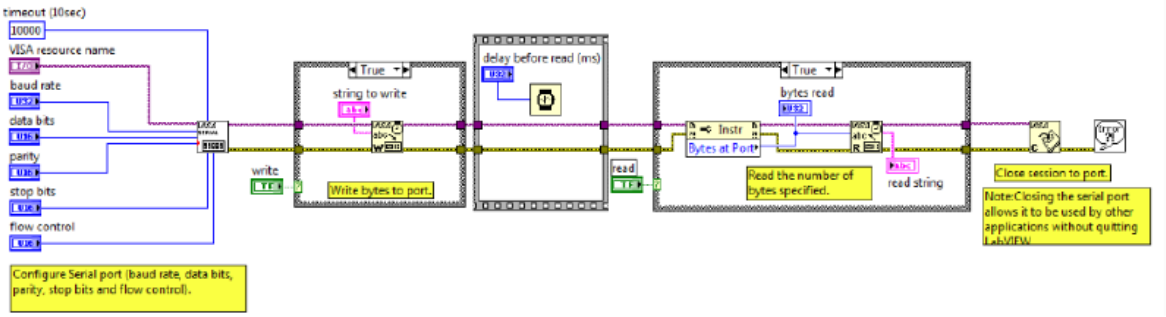

Work flow chart of robotic communication